Applied Catalysis B: Environmental 296 (2021) 120322

Contents lists available at ScienceDirect

Applied Catalysis B: Environmental

journal homepage: www.elsevier.com/locate/apcatb

Enhancing the CO_2 methanation activity of γ-Al_2O_3 supported mono- and bi-metallic catalysts prepared by glycerol assisted impregnation

Adrián Quindimil [a], M. Carmen Bacariza [b], José A. González-Marcos [a], Carlos Henriques [b,*], Juan R. González-Velasco [a,*]

[a] Departamento de Ingeniería Química, Facultad de Ciencia y Tecnología, Universidad del País Vasco UPV/EHU, Barrio Sarriena, 48940, Leioa, Bizkaia, Spain
[b] Centro de Química Estructural, Instituto Superior Técnico, Universidade de Lisboa, Av. Rovisco País, 1049-001, Lisboa, Portugal

ARTICLE INFO

Keywords:
Glycerol assisted impregnation
Ni-Ru bimetallic catalyst
CO_2 methanation
Reaction mechanism
Operando FTIR

ABSTRACT

Conventional Ni/Al_2O_3 catalyst, currently used for CO_x removal in ammonia production, admits room for improvement as catalysts for application in low temperature CO_2 methanation, which is the aim of this work. The Incipient Wetness Impregnation (IWI) has been replaced by Glycerol Assisted Impregnation (GAI) method and, afterwards, a secondary metal (Ru) has been co-impregnated forming a bimetallic system. The monometallic as well as bimetallic systems have been characterized by several techniques (TGA, XRD, N_2-physisorption, TEM, H_2-TPR, H_2-TPD, STEM-EDX and *operando* FTIR) and tested for CO_2 methanation reaction in a downflow fixed bed reactor (conditions: P =1 bar, H_2: CO_2 ratio = 4 and WHSV = 30,000 mL h^{-1} g^{-1}). GAI method together with a reducing calcination atmosphere (20 %H_2/N_2) results effective to avoid the formation of large metal particles during the synthesis, especially for Ru/Al_2O_3 formulation. In fact, the Ru dispersion of the catalyst prepared by GAI ($RuAl_{GAI}$) is around 5 times higher than that of $RuAl_{IWI}$ catalyst. On the other hand, $NiAl_{GAI}$ presents larger population of reduced particles but bigger in size than $NiAl_{IWI}$ catalyst, which finally provides the former with slightly higher metal surface and superior catalytic performance. By co-impregnating small amounts of Ru (0.5, 1.0 or 1.5 wt%) the Ni surface is considerably increased which, together with Ru synergistic collaboration, results in a methane yield rise from 20 to 44 % at 300 °C. The operando FTIR results show no differences in the reaction pathway with GAI preparation method and incorporation of Ru, but different evolution of reaction intermediates concentration with temperature. The bimetallic Ni-RuAl system presents much higher capacity to adsorb CO and hydrogenate the reaction intermediates (adsorbed formates and carbonyls) by dissociated H_2 than its monometallic counterparts.

1. Introduction

Global anthropogenic CO_2 emissions were reduced about 8% (2.6 Gt of CO_2) in 2020, as a result of the Covid-19 crisis [1]. This fact, although results from lockdown measures and economy slowdown, may turn into the starting point from which CO_2 emissions progressively decline in the future if adequate actions are taken. According to IEA, governments have now the chance to accelerate the transition into a more resilient and cleaner energy system, while rebooting their economies and creating new jobs. Making the right investments, the economic growth can work together with a sustainable recovery plan, which might lead to air pollution emissions decrease of 5% by 2023 [2]. This plan, among other objectives, contemplates: (i) accelerating the installation of low carbon energy sources (such as renewable wind and solar PV) along with the expansion and modernisation of electricity grids; (ii) turn fuels production and utilization more sustainable; and (iii) boost innovation in crucial technology areas including hydrogen, batteries, CO_2 utilisation and small modular nuclear reactors. In this context, Power to Gas (PtG) process is presented as an interesting alternative. This process targets the production of synthetic natural gas (SNG) through the catalytic conversion of renewably produced H_2 and CO_2 from flue gases according to the Sabatier reaction: $CO_2 + 4H_2 \rightleftarrows CO_2 + 2\,H_2O$ (ΔH° = -165 kJ mol^{-1}). Thus, CO_2 is used as raw material instead of being emitted as a waste and renewable energy is stored in form of a low-carbon fuel such as SNG or methane. Besides, as H_2 is produced via water electrolysis in low electricity demand periods, renewable power is better exploited, which promotes its development and expansion. The produced CH_4 can be easily stored or widely distributed in the current

* Corresponding authors.
E-mail addresses: carlos.henriques@ist.utl.pt (C. Henriques), juanra.gonzalezvelasco@ehu.es (J.R. González-Velasco).

https://doi.org/10.1016/j.apcatb.2021.120322
Received 2 February 2021; Received in revised form 23 April 2021; Accepted 5 May 2021
Available online 7 May 2021

gas grid and, afterwards, can be used again for power and heat generation in private homes, mobility sector or industry [3,4].

The complete hydrogenation of CO_2 into methane (popularly named as CO_2 methanation) is a process with considerable kinetic limitations (8 electron reduction) which can only be achieved with a suitable catalyst; commonly, supported Ni or Ru highly dispersed over a basic mesoporous support. In recent years, Ni and Ru catalysts with increasingly smaller and, *a priori*, more active metallic particles have been designed mostly due to advances in nanomaterials synthesis techniques, which allow increasing the surface/volume ratio and the number of active sites [5,6]. The reduction of particle size not only leads to higher metallic surface areas but also to changes in particle's morphology, which according to its structure sensitivity could modify Turnover Frequency (*TOF*) numbers. It has been reported that low coordinated Ni nanoparticles contain more surface defects that act as surface hydrogen traps facilitating its dissociation and improving Ni specific activity [7]. On the contrary, other authors have reported that, in the case of Ru catalysts, low coordinated or monolayer sites induce lower CO_2 methanation rates than larger nanoclusters, since they suffer from poisoning by the adsorption of stable carbonyls during reaction [8–10]. In order to obtain small particles or change their structure, diverse preparation methods have been alternatively employed, such as Incipient Wetness Impregnation (IWI) [11], one-pot Evaporation-Induced Self-Assembly (EISA) [12], Microwave-Assisted (MA) [13], Deposition-Precipitation (DP) [14], Co-Precipitation (CP) [15] and polyol method [16] or equivalent Glycerol Assisted Impregnation (GAI) [17].

The main disadvantage of Ni catalysts with respect to those of Ru is their considerably lower activity at low temperature due to their inferior H_2 dissociation capacity [18]. Instead, the main drawback of Ru catalysts is their exorbitant price. Nevertheless, designing appropriate Ni-Ru bimetallic systems could be a solution to balance those handicaps. Generally, these bimetallic catalysts are known to exhibit better catalytic properties compared to their monometallic counterparts such as higher conversion, fewer side reactions (selectivity) and more stability due to a synergistic effect [19–21]. This synergy happens as a result of specific electronic interactions and geometric positional relationships between the two metals (combination of "ligand" and "ensemble" effects) [20]. By adding an appropriate secondary metal (Ru) to the catalytic formulation, the electronic properties of the main metal (Ni) are usually altered leading to changes in reagents adsorption and reaction intermediates formation. These changes, in turn, can modify the reaction pathway and the activation energy so that the activity of the catalyst is improved [21]. Recently, Ni-Ru bimetallic systems have proven to be very effective specifically for CO methanation [22–25]. Liu et al. [26] also reported enhanced catalytic activity for CO_2 methanation over 10Ni-1Ru-2CaO/Al_2O_3 formulation due to a significant increase in H_2 and CO_2 chemisorption capacities, whereas Wei et al. [27] did not achieve activity improvement by adding Ru to Ni-zeolite (13X and 5A) catalysts. However, the analysis of Ni-Ru systems in terms of physicochemical and catalytic properties for CO_2 methanation has not been the focus of many systematic studies so far.

Regarding CO_2 methanation reaction mechanism, several studies have been carried out by means of *Operando* FTIR or DRIFTS with the aim of determining the reaction intermediates and elementary reaction steps over supported Ni [20,28–30] and Ru [9,10,16,31] catalysts. Although there is still controversy regarding the identification and the role or place of some adsorbed species in the reaction pathway, two widely accepted routes have been proposed: the so-called dissociative and associative mechanisms [32]. The former assumes the dissociative adsorption of CO_2 into adsorbed CO or carbonyl followed by its hydrogenation into CH_4. In the latter, by contrast, CO_2 is molecularly adsorbed in form of carbonates or bicarbonates, which are progressively reduced by H spillover into formate, methoxy species and, finally, methane [33]. Noteworthy, CO_2 methanation mechanism over bimetallic catalysts has scarcely been studied.

The main goal of this work has been to sequentially improve the low temperature activity of the conventional and industrial Ni/Al_2O_3 formulation by modifying the preparation method and incorporating a secondary metal, such as Ru. Additionally, this work has aimed to identify which factors are responsible for such improvement. Firstly, the influence of Glycerol Assisted Impregnation (GAI) method on the dispersion and structural characteristics of Al_2O_3-supported Ni and Ru particles was examined. These materials were catalytically compared with equivalent ones prepared by the conventional Incipient Wetness Impregnation method (IWI). After that, the effect of Ru incorporation on the physicochemical properties and catalytic performance of Ni/Al_2O_3 formulation was studied. To our knowledge, we pioneer operando FTIR analysis of CO_2 methanation reaction on Ni-Ru bimetallic system, identifying the type and evolution of reaction intermediates and determining the roles of both Ni and Ru in the reaction pathway.

2. Experimental

2.1. Catalysts preparation

For this work, a series of alumina-supported Ni and Ru catalysts as well as bimetallic Ni-Ru/Al_2O_3 samples were prepared. The two pairs of monometallic Ni and Ru catalysts were obtained by two synthesis procedures that consisted of the following steps: impregnation and calcination. According to the first procedure, the metal (Ni or Ru) nitrate solution was incorporated into Al_2O_3 support by Incipient Wetness Impregnation (IWI) and the resulting catalyst precursor was calcined in a muffle under air (uncontrolled atmosphere). IWI method as well as calcination procedure was the same as followed and explained in detail in our previous work [34]. However, in the second synthesis route, the metal solution is introduced by Glycerol Assisted Impregnation (GAI) method and the precursor is calcined under a controlled atmosphere. The GAI method, which was developed by Gudyka et al. [17], also consists of the typical dry impregnation but employs a glycerol/water solution as solvent instead of bare H_2O. In our case, a 30 wt% $C_3H_8O_3$/water solution was used. After impregnation, samples were dried overnight and calcined *ex situ* in a tubular reactor under 50 mL min^{-1} of 20 %H_2/N_2 (controlled atmosphere) at 550 °C for 2 h (with 10 °C min^{-1} heating rate). In both cases, the required amounts of Ni $(NO_3)_2{\cdot}6H_2O$ *(Sigma Aldrich,* 99.99 %*)* and $Ru(NO)(NO_3)_3$ *(Sigma Aldrich, Ru* = 1.5 % *w/v)* precursors were employed in order to attain 12 wt% Ni and 3 wt% Ru nominal metal contents and the calcination temperature was chosen according to thermogravimetric results of catalysts precursors. These four catalysts were labelled according to their composition and preparation method as follows: $NiAl_{IWI,}$ $RuAl_{IWI}$, $NiAl_{GAI}$ and $RuAl_{GAI}$.

On the other hand, once results of monometallic catalysts were analysed, three additional bimetallic catalysts were prepared by GAI method varying the Ru content from 0.5 to 1.5 wt%. In all cases, the nominal Ni content was set at 12 wt% and small amounts of Ru were incorporated by co-impregnation. After that, samples were also dried overnight at 120 °C and calcined under the same conditions described above. These samples were named Ni-xRuAl, where variable x represents the Ru content (0.5, 1.0 or 1.5 wt%).

2.2. Characterization techniques

In order to determine the suitable calcination temperatures, thermogravimetric analysis was carried out in a Setaram Setsys Evolution apparatus connected in series with a Pfeiffer Prisma mass spectrometer (TGA-MS). In all cases, around 100 mg of catalyst precursor was placed in a 30 μL Al_2O_3 crucible and was firstly dried *in situ* at 125 °C. After that, the temperature was increased from 125 to 625 °C with 5 °C min^{-1} heating rate and continuously recorded along with mass loss. The catalysts precursors prepared by IWI method were calcined under 50 mL min^{-1} oxidative stream (5% O_2/He), whereas the ones prepared by GAI were analysed under reductive atmosphere (5% H_2/Ar). The exit gas

stream composition was analysed by mass spectrometry following the 16 (CH_4), 17 (NH_3), 18 (H_2O), 28 (CO/N_2), 30 (NO), 44(CO_2/N_2O) and 46 (NO_2) mass signals.

The textural properties and crystalline phases of the supported catalysts were determined by N_2 physisorption and X Ray Diffraction (XRD). The protocols for these analyses are detailed in the former work [34].

The micrographs of the monometallic catalysts were obtained by a TECNAI G2 20 TWIN microscope which operates at 200 kV and is equipped with a LaB_6 filament, EDAX-EDS microanalysis system and Transmission Electron Microscopy (TEM). The micrographs together with elemental maps of the bimetallic catalysts, instead, were taken by a FEI Titan Cubed G2 60–300 microscope with much higher resolution. This microscope is equipped with a high-brightness X-FEG Schottky field emission electron gun, monochromator, CEOS Gmbh spherical aberration corrector and Super-X EDX system with High-Angle Annular Dark-Field (HAADF) detector for Z contrast imaging in Scanning Transmission Electron Microscopy (STEM) configuration. All powder samples were mixed with ethanol solvent and kept in and ultrasonic bath for 15 min in order to attain a good suspension. After that, a drop of suspension was spread onto a TEM copper grid (300 mesh) covered by a holey carbon film for each sample. Finally, the grids were dried under vacuum to remove the solvent. The particle size distribution of monometallic catalysts was determined by measuring the diameter (d) of at least 200 particles. After that, the mean metal dispersion (D_{Me}) was estimated applying the d-FE model [35] as follows:

$$D_{\mathrm{Me}}(\%) = \frac{5.01 d_{at} \sum_j n_j d_j^2 + 2.64 d_{at}^{0.81} \sum_k n_k d_k^{2.19}}{\sum_i n_i d_i^2} \times 100 \quad (1)$$

where, d_i, d_j and d_k are the diameters of the "i", "j" and "k" particles, n_i is the number of particles with diameter d_i, n_j is the number of particles with diameter d_j ($d_j > 24 \cdot d_{at.}$), n_k is the number of particles with diameter d_k ($d_k \leq 24 \cdot d_{at}$) and $d_{at.}$ is the atomic diameter of Ni or Ru.

The resistance against oxidation of catalysts prepared by GAI method was determined by three consecutive RedOx cycles in a Micromeritics AutoChem 2920 apparatus. Previously, the samples were exposed to a 50 mL min^{-1} stream of 5%H_2/Ar in order to reduce the passivated nickel layer. For each RedOx cycle, 15 oxidative pulses (5 cm^3 of 5%O_2/He) were injected followed by another 15 reductive pulses (5 cm^3 of 5%H_2/Ar). Note that between pulse injections an inert gas stream of He or Ar was continuously fed depending on the step (oxidative or reductive, respectively). The resistance to oxidation of $NiAl_{GAI}$ and Ni-1.0RuAl catalysts was measured at 325 °C, while that of $RuAl_{GAI}$ catalyst at 550 °C. The temperatures were chosen considering that Ni and Ru are oxidized at around 300 °C and 500 °C, respectively [19]. The resistance against oxidation, defined as the cycle reversibility, was calculated by the following expression:

$$\text{Reversibility of cycle}_i(\%) = \frac{n_i(\mathrm{Ni^0})}{n_i(\mathrm{Ni^{2+}}) + n_{i-1}^{\mathrm{rem.}}(\mathrm{Ni^{2+}})} \times 100 \quad (2)$$

where, $n_i(Ni^{2+})$ are the moles of Ni oxidized in cycle i, $n_{i-1}^{\mathrm{rem.}}(Ni^{2+})$ are the moles of Ni that remain oxidized from previous cycles and $n_i(Ni^0)$ are the moles of Ni reduced or recovered in cycle i. Note that $n_i(Ni^{2+})$ as well as $n_i(Ni^0)$ were calculated from total O_2 and H_2 uptakes of oxidative and reductive steps, respectively.

Hydrogen Temperature Programmed Desorption (H_2-TPD) experiments were also performed on a Micromeritics AutoChem 2920 apparatus. These experiments allowed us determining the hydrogen chemisorption capacity as well as chemisorption strength of monometallic and bimetallic catalysts. In a first step, the metal surface of samples was reduced and cleaned up by 5%H_2/Ar gas stream at 500 °C for 30 min and then cooled down to 50 °C. After that, a 50 mL min^{-1} stream of pure hydrogen was fed long enough for complete adsorption or saturation (around 1 h). Subsequently, catalysts were flushed out with Ar for 30 min in order to remove physisorbed H_2. Finally, the desorption was conducted increasing temperature up to 850 °C at 10 °C min^{-1} heating rate. From integration of TPD profiles at T < 450 °C, the metallic surface area (S_{Ni}) of $NiAl_{GAI}$ catalyst was estimated according to this equation:

$$S_{\mathrm{Ni}}\left(\mathrm{m^2 g^{-1}}\right) = \frac{N_A}{V_m} \times V_{\mathrm{des.}} \times SF \times atA_{\mathrm{Ni}} \quad (3)$$

where, N_a is the Avogadro number, V_m is the molar volume in cm^3 mol^{-1}, $V_{des.}$ is the volume in cm^3 of desorbed H_2 per gram of catalyst, SF is the stoichiometric factor and atA_{Ni} is the effective atomic area of Ni. In this work, a SF (Ni/H_2) of 2 and atA_{Ni} of 6.49 × 10^{-20} m^2 $atom^{-1}$ were assumed.

2.3. Catalytic activity

CO_2 methanation reaction was performed in a downstream fixed bed reactor (ID =9 mm). In all cases, the stainless-steel reactor was loaded with 0.5 g of catalyst particles (d_p = 300−500 μm), which were diluted to 50 % (v/v) with quartz particles in order to avoid hot spots. The Ni and Ru catalysts prepared by IWI were firstly reduced at 500 and 400 °C for 1 h with 20 % H_2/He, respectively. The samples prepared by GAI were also reduced but at 250 °C in order to remove the passivated oxide layer formed by having been in contact with air. After cooling down the samples to 200 °C with He (inert gas), the temperature was raised up to 400 °C in steps of 25 °C under reactant stream. This gaseous mixture was composed of 16 % CO_2 and 64 % H_2 ($H_2/CO_2 = 4$), balanced up to 100 % with He (total flow of 250 cm^3 min^{-1}). The outlet gas stream composition was analysed by GC (Agilent 7890B) once steady state was reached at each temperature. H_2, He, CH_4 and CO concentrations were monitored by MolSieve type columns, while that of CO_2 by HayeSep type column. The produced water was retained by a Peltier cooling module upstream of the gas chromatograph to avoid molecular sieve column degradation. All reactions were carried out at atmospheric pressure and at WHSV of 30,000 mL h^{-1} g_{cat}^{-1}.

The catalytic performance was evaluated by CO_2 conversion (X_{CO_2}), CH_4/CO products selectivity (S_{CH_4} or S_{CO}) and yield (Y_{CH_4} and Y_{CO}) which were calculated from reactor inlet and outlet molar flows according to the following equations:

$$X_{\mathrm{CO_2}}(\%) = \frac{F_{\mathrm{CO_2}}^{\mathrm{in}} - F_{\mathrm{CO_2}}^{\mathrm{out}}}{F_{\mathrm{CO_2}}^{\mathrm{in}}} \times 100 \quad (4)$$

$$S_{\mathrm{CH_4}}(\%) = \frac{F_{\mathrm{CH_4}}^{\mathrm{out}}}{F_{\mathrm{CO_2}}^{\mathrm{in}} - F_{\mathrm{CO_2}}^{\mathrm{out}}} \times 100 \quad (5)$$

$$S_{\mathrm{CO}}(\%) = \frac{F_{\mathrm{CO}}^{\mathrm{out}}}{F_{\mathrm{CO_2}}^{\mathrm{in}} - F_{\mathrm{CO_2}}^{\mathrm{out}}} \times 100 \quad (6)$$

$$Y_{\mathrm{CH_4}}(\%) = X_{\mathrm{CO_2}} \times \frac{S_{\mathrm{CH_4}}}{100} = \frac{F_{\mathrm{CH_4}}^{\mathrm{out}}}{F_{\mathrm{CO_2}}^{\mathrm{in}}} \times 100 \quad (7)$$

$$Y_{\mathrm{CO}}(\%) = X_{\mathrm{CO_2}} \times \frac{S_{\mathrm{CO}}}{100} = \frac{F_{\mathrm{CO}}^{\mathrm{out}}}{F_{\mathrm{CO_2}}^{\mathrm{in}}} \times 100 \quad (8)$$

where F_i is the inlet or outlet molar flow of component "i" in mol s^{-1}.

Finally, the Turnover Frequency (TOF) numbers, which indicate the number of CO_2 molecules converted per second and per active site, were calculated as follows:

$$TOF_{Me}\left(\mathrm{s^{-1}}\right) = \frac{-r_{\mathrm{CO_2}}\left(\mathrm{mol\ CO_2 g_{cat.}^{-1}\ s^{-1}}\right)}{S_{Me}\left(\mathrm{mol\ Me g_{cat}^{-1}}\right)} = \frac{F_{\mathrm{CO_2}}^{\mathrm{in}} \times X_{\mathrm{CO_2}} \times MW_{Me}}{W \times D_{Me} \times F_{Me}} \quad (9)$$

where MW is the mass weight of the metal in g mol^{-1}, W is the catalyst weight in g, D_{Me} is the metallic dispersion and F_{Me} is the mass fraction of metal in the catalyst.

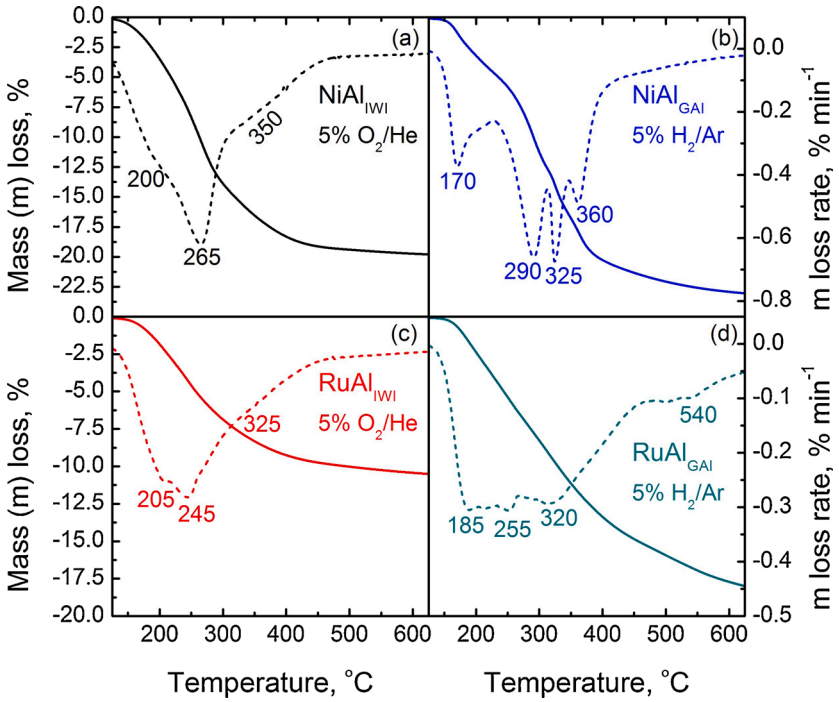

Fig. 1. TG (continuous line) and dTG (discontinuous line) profiles of (a, b) Ni and (c, d) Ru catalysts precursors under oxidative (5% O_2/He) and reductive (5% H_2/Ar) calcination atmospheres.

2.4. Operando FTIR measurements

Operando FTIR spectra were collected using an IR cell from In-Situ Research Instruments, coupled to a Nicolet 6700 spectrometer equipped with a MCT detector and using a spectra resolution of 4 cm^{-1}. Powdered samples were pressed at 1.5 tons into 10 mg cm^{-2} wafers which, prior to the experiments, were *in situ* activated/reduced at 500 °C for 1 h under a 5% H_2/Ar flow of 20 mL min^{-1}. After pretreatment, wafers were cooled down under Ar flow to 150 °C, being background spectra collected every 25 °C. CO_2 adsorption tests were carried out by exposing samples to a 20 mL min^{-1} stream of 5% CO_2/Ar, whereas in CO_2 methanation experiments a 5% CO_2: 20 % H_2: 75 % Ar gas mixture was used. In both cases, experiments were carried out in two steps. Firstly, the used gas mixture was stabilised during 30 min and a series of spectra were collected at 0, 1, 3, 5, 10, 15 and 30 min. Secondly, temperature programmed adsorption (CO_2/Ar flow) or temperature programmed surface reaction (TPSR, CO_2/H_2/Ar flow) was run from 150 to 450 °C using a heating rate of 2 °C min^{-1}. Note that the depicted spectra were obtained by subtraction of those recorded under reaction/adsorption conditions every 25 °C and those corresponding to backgrounds.

3. Results

3.1. Influence of the preparation method

To determine how catalysts precursors are decomposed and the temperature required for their complete calcination, thermogravimetric analysis (TGA) was carried out (Fig. 1). Additionally, the gaseous products from precursors calcination were analysed by a mass spectrometer connected at the exit of the thermobalance (Figs. S1 and S2, supplementary material). Fig. 1a and b show both TG and dTG profiles of supported Ni catalysts precursors calcined under oxidative (5% O_2/He, IWI catalyst) and reductive (5% H_2/Ar, GAI catalyst) atmospheres, respectively. In general, the mass loss takes place in different consecutive steps that can be identified by the dTG profiles. In the case of $NiAl_{IWI}$ precursor calcined under O_2/He (Fig. 1a), the dTG profile presents a main mass loss rate peak at 265 °C and two shoulders at 200 and 350 °C. The first shoulder can be attributed to structural water desorption from Al_2O_3 or water released during dehydration steps of nickel precursor ($Ni(NO_3)_2{\cdot}6H_2O$), whereas the broad peak and the second shoulder are due to nitrate decomposition/oxidation into NO_x (NO and NO_2), as confirmed by MS signals (Fig. S1b). Mass loss is observed up to 475 °C approximately, suggesting that a calcination temperature of 500 °C is enough for the complete precursor decomposition into NiO/Al_2O_3.

The TG profile of the $NiAl_{GAI}$ precursor (Fig. 1b) is somewhat different due to the presence of an organic compound which could be a metal alkoxide from coordination nickel cations (Ni^{2+}) with glycerol solution [5,6,17]. In this case, the dTG profile shows 4 differentiated negative peaks among 125 and 400 °C. In agreement with MS spectra (Fig. S1d), the first one at 170 °C could be attributed to NO_3^- reduction into NO and the next two, centered at 290 and 325 °C, to the reduction of the organic template. It can be suggested that the glycerolate is decomposed into smaller molecules (such as ethylene glycol and ethanol) and surface carbon by hydrogenolysis reactions. In fact, the last mass loss rate peak centered at 360 °C matches with the appearance of methane (m/z = 15) in the product stream, suggesting that the remaining surface carbon is being reduced. In this case and according to the TG profile, a calcination temperature of 550 °C is needed to complete $NiAl_{GAI}$ precursor reduction.

Regarding Ru/Al_2O_3 precursors, the TGA profiles of their respective calcinations are shown in Fig. 1c and d. By comparing those figures with the above described, it can be observed that the mass loss profile of $RuAl_{IWI}$ precursor (Fig. 1c) is similar to that of $NiAl_{IWI}$ (Fig. 1a). In fact, the same calcination steps are identified and confirmed by MS spectra (Fig. S2b): a first peak at 205 °C due to water release followed by a more intense negative peak together with a shoulder at 335 °C, which are attributed to nitrate and nitrosyl groups oxidation into NO_x. Although the precursor is completely removed at 450 °C, a calcination temperature somewhat lower (400 °C) was employed in order to avoid excessive growing of RuO_2 crystallites [34]. Finally, TGA profiles of $RuAl_{GAI}$ precursor calcined under 5%H_2/Ar are shown in Fig. 1d. Note that the dTG profile presents a broad band which could be divided into 3 negative peaks at 185, 255 and 320 °C, which correspond to several

Table 1
Physicochemical and catalytic properties of monometallic catalysts.

Catalyst	Metal cont. (%)[a]	S_{BET} ($m^2\ g^{-1}$)[b]	V_{pore} ($cm^3\ g^{-1}$)[b]	τ (nm)[c]	D_{Me} (%)[d]	S_{Me} ($m^2\ g^{-1}$)[d]	TOF (s^{-1})[e]	TOF/I_0 ($m^2_{surf.}\ m^{-1}_{int.}\ s^{-1}$)[f]
$NiAl_{IWI}$	11.2	166	0.373	4.8	19.8	5.62	$1.12{\cdot}10^{-2}$	$3.22{\cdot}10^{-11}$
$NiAl_{GAI}$	10.8	160	0.362	9.7	11.5	8.25	$1.04{\cdot}10^{-2}$	$1.39{\cdot}10^{-11}$
$RuAl_{IWI}$	3.0	202	0.430	11.0	7.2	0.79	$2.03{\cdot}10^{-1}$	$4.84{\cdot}10^{-10}$
$RuAl_{GAI}$	3.1	198	0.412	< 5	34.4	3.90	$7.39{\cdot}10^{-2}$	$6.90{\cdot}10^{-12}$

[a] Determined by ICP.
[b] Calculated by BET equation and t-Plot method.
[c] XRD crystallite size estimated by Scherrer equation.
[d] Estimated from TEM micrographs.
[e] Turnover Frequency calculated by Eq. 9.
[f] Specific activity normalized with respect to interfacial length by Eq. 10.

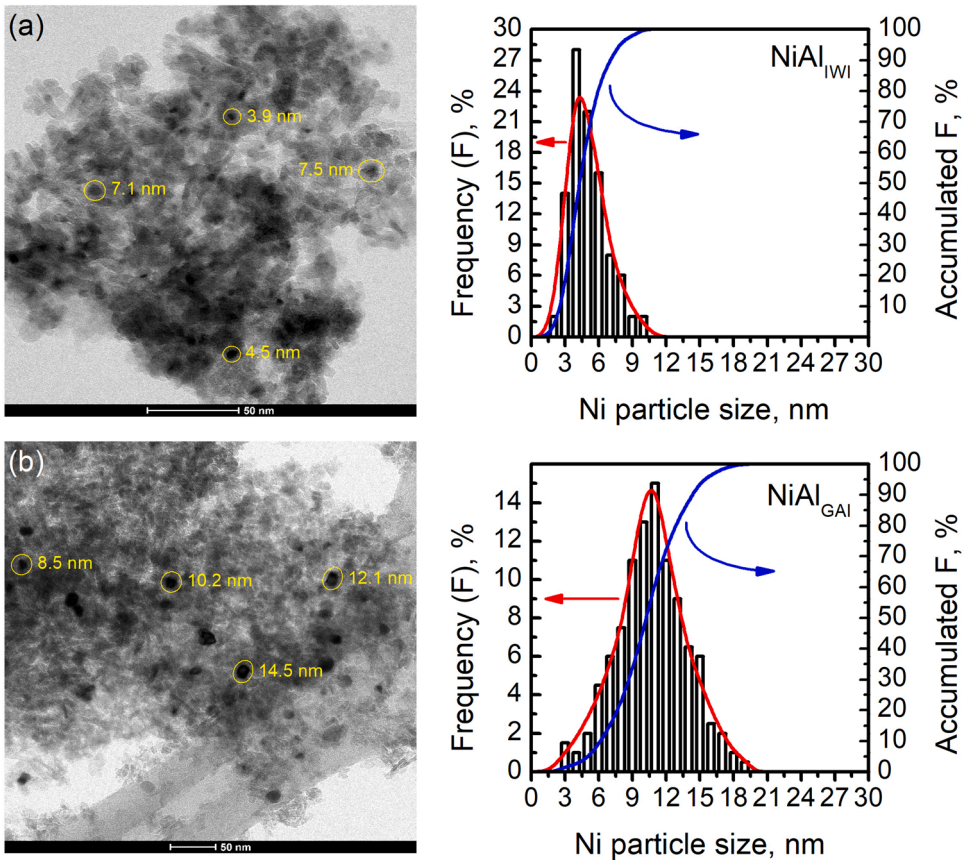

Fig. 2. TEM micrographs along with particle size distributions of (a) $NiAl_{IWI}$ and (b) $NiAl_{GAI}$ catalysts.

calcination steps. According to MS spectra (Fig. S2d), nitrate groups and organic compounds are partially reduced and water is released as product in a first step (negative peak at 190 °C). In a second step (from 250 to 350 °C), the organic compound continues being reduced and carbon monoxide (m/z = 28) is observed in the products stream. Additionally, a small broad peak can be appreciated at around 540 °C. This peak matches with methane appearance from hydrogenation of remaining surface carbon. In this case, a temperature of 550 °C was used for precursor calcination. It must be highlighted that in all cases the observed total mass loss is similar to that expected for complete calcination of catalyst precursors: 19.9 vs. 17.2 % for $NiAl_{IWI}$, 23.5 vs. 27.1 % for $NiAl_{GAI}$, 10.9 vs. 9.9 % for $RuAl_{IWI}$ and 18.9 vs. 19.6 % for $RuAl_{GAI}$.

Once catalysts precursors were calcined according to TGA results, the resulting catalysts were characterized by several techniques. Some physicochemical properties are shown in Table 1. It should be noted that the metal content of all catalysts is close to the nominal, indicating that Ni and Ru were successfully incorporated by the two methods (IWI and GAI). In addition, the high specific surface area and pore volume of all catalysts indicate that the textural properties of starting γ-Al_2O_3 (S_{BET} = 214 $m^2\ g^{-1}$ and V_{pore} = 0.563 $cm^3\ g^{-1}$) were not considerably affected by the different impregnation and calcination processes. As expected, supported Ni catalysts presented lower S_{BET} and V_{pore} than RuAl ones, mainly due to their higher metal content. On the other hand, the catalysts prepared by GAI method exhibited slightly lower values of such textural properties than those prepared by IWI, probably due to the higher calcination temperature.

In regard to XRD analysis of reduced catalysts (not shown), both elemental Ni (XRD peaks at 2θ = 44.5, 51.8 and 76.4 °) and Ru (XRD peaks at 2θ = 38.4, 42.2 and 44 °) were clearly identified on $NiAl_{GAI}$ and $RuAl_{IWI}$ samples, respectively. However, broad and low-intensity peaks of Ni^0 and no peaks of Ru^0 were detected in $NiAl_{IWI}$ and $RuAl_{GAI}$ XRD patterns, suggesting that the crystalline phases are better dispersed than on $NiAl_{GAI}$ and $RuAl_{IWI}$ catalysts. This fact was confirmed by crystallite size calculation according to Scherrer equation (τ, Table 1).

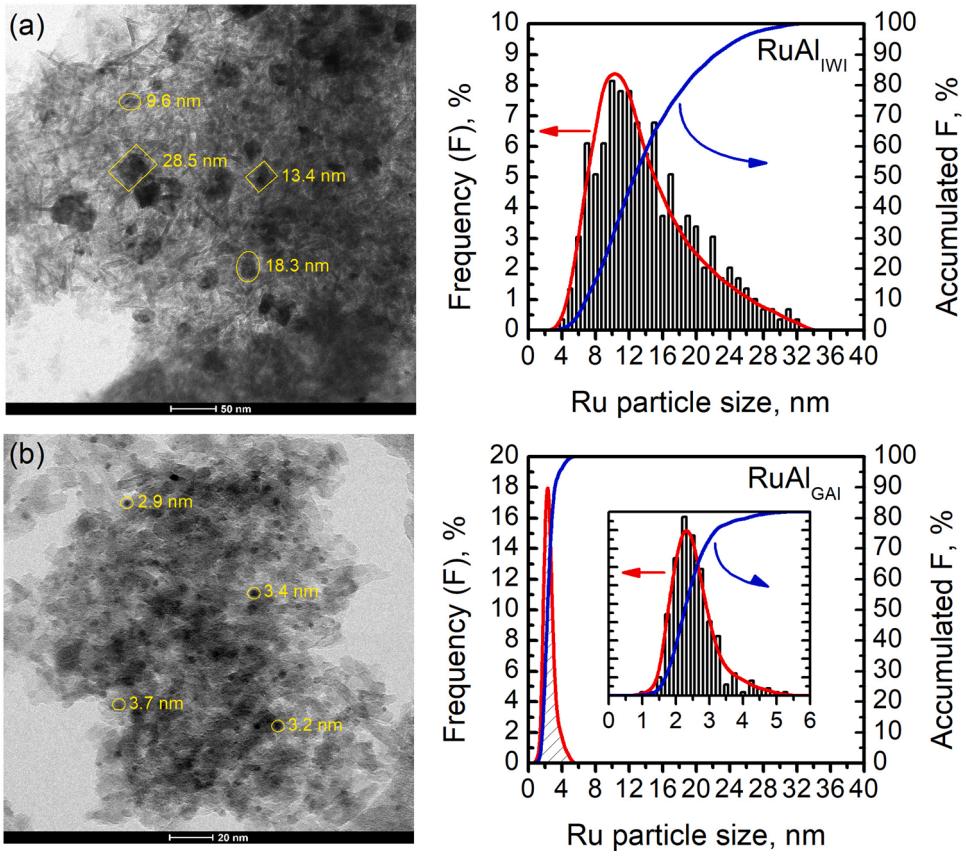

Fig. 3. TEM micrographs along with particle size distributions of (a) $RuAl_{IWI}$ and (b) $RuAl_{GAI}$ catalysts.

The effect of the preparation method on the morphology as well as on the particle size distribution was determined by TEM. In addition, the mean metal dispersion and metal surface area (Table 1) were calculated by d-FE model [35]. The micrographs of Ni catalysts along with their corresponding particle size distribution histograms are displayed in Fig. 2. In both cases, quasi-spherical supported Ni particles (circled in yellow) were observed. It can be appreciated that the particle size distribution (calculated from measurement of at least 200 particles) is wider in the case of the sample prepared by GAI method. In fact, $NiAl_{IWI}$ catalyst presents Ni particles sizes from 2 to 10 nm, whereas the distribution of $NiAl_{GAI}$ sample ranges from 3 to 19 nm. In this line, the average particle sizes are 5.8 nm (D_{Ni} = 19.8 %) and 11.2 nm (D_{Ni} = 11.5 %) for $NiAl_{IWI}$ and $NiAl_{GAI}$ catalysts, respectively. Note that these values are in agreement with crystallite sizes estimated by XRD, indicating that the active phase is better dispersed on $NiAl_{IWI}$ catalyst. However, this catalyst presents a reduction degree of 38 % at 500 °C, i.e., less than the half of total nickel is reduced before the reaction, as determined in our previous work [34]. For that reason, the Ni reactive surface area is slightly higher for the catalyst prepared via GAI method (see Table 1).

Such differences in dispersion and amount of reducible nickel are related with the calcination step. In the case of $NiAl_{IWI}$ catalyst, the precursor is calcined in air favouring mainly the formation of NiO highly interacting with the support or even $NiAl_2O_4$ inert phase. After reduction treatment at 500 °C, small and well distributed Ni particles are obtained but not all nickel is reduced due to the high metal-support interaction observed by H_2-TPR. This high interaction between NiO and Al_2O_3, which was extensively studied in the literature [36,37], is also confirmed by examination and comparison of several TEM micrographs: far fewer Ni particles are visualized on $NiAl_{IWI}$ than on $NiAl_{GAI}$ catalyst, indicating a lower Ni reduction extent. On the other hand, the $NiAl_{GAI}$ precursor is calcined under reductive atmosphere (20 % H_2/N_2), avoiding the formation of Ni^{2+} species able to react with γ-Al_2O_3 and assuring that all nickel will be reduced after the preparation procedure. Besides, the presence of non-volatile organic compounds apparently prevents Ni crystals from excessive growing. As the temperature increases during the calcination, it seems that incipient nickel nanocrystals are embedded in an organic matrix that acts as a barrier preventing them from sintering [17]. As a result, all Ni is reduced and quite well dispersed in form of 11 nm size particles. Noteworthy, Ding et al. [38] observed a similar Ni particle size distribution for a Ni/SiO_2 prepared by the glycerol assisted impregnation and reported that glycerol resulted to be the best alkanol solvent among those studied.

Analogously, Fig. 3 shows TEM micrographs together with particle size histograms of monometallic Ru/Al_2O_3 samples. In both catalysts, Ru particles with different morphology were easily visualized (within yellow circles or rectangles). Ruthenium was homogeneously dispersed in form of spherical particles on $RuAl_{GAI}$ while a much more heterogeneous distribution was verified on $RuAl_{IWI}$. The latter presents both oval and hexagonal Ru particles or even aggregates formed by several particles. In this case, the particle size distribution seems to be quite affected by the preparation method. On one side, $RuAl_{IWI}$ catalyst has an unimodal particle size distribution with a long tail ranging from 4 to 32 nm and a corresponding average particle size of 14.8 nm (D_{Ru} = 7.2 %). On the contrary, the particle size distribution of $RuAl_{GAI}$ sample, shown in Fig. 3b, is symmetric and much narrower. It should be noted that this catalyst presents an average particle size of 2.7 nm, which correspond to a dispersion of 34.4 %. These results clearly indicate that GAI is a more appropriate method to disperse Ru over Al_2O_3.

In our former studies based on thermo-XRD results, we reported that RuO_2 crystals tend to grow fast and agglomerate under oxidative calcination conditions due to the formation of volatile RuO_x [34]. That would explain why bigger particles and so long tail are observed in the histogram of the catalyst prepared by IWI method. This fast growth is clearly avoided by GAI method, which includes a non-oxidative

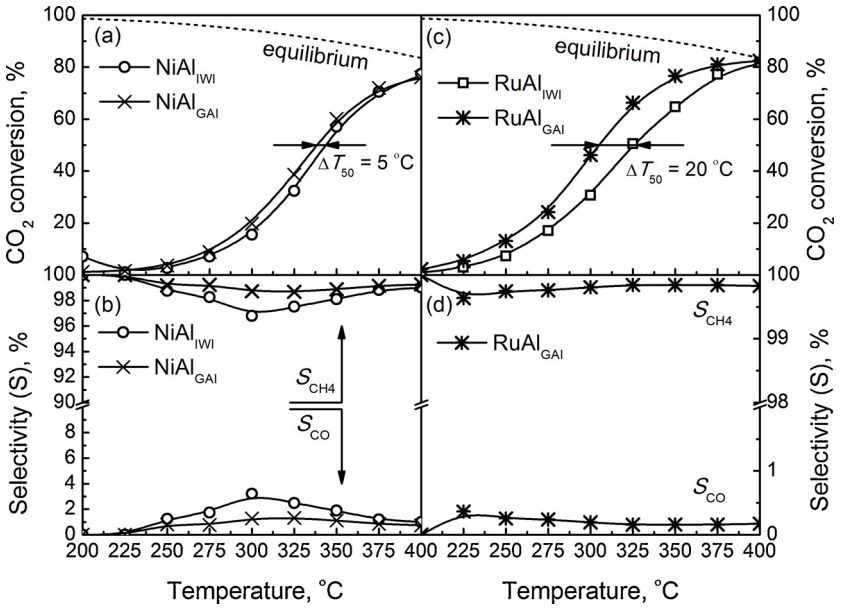

Fig. 4. Light-off curves together with products (CH_4 and CO) selectivity profiles of (a, b) Ni and (c, d) Ru catalysts. Reaction conditions: P =1 bar, H_2: CO_2 ratio = 4 and WHSV = 30,000 mL h^{-1} g_{cat}^{-1}.

calcination. Furthermore, even more uniform and smaller particles are created due to the organic enclosing effect above explained. Yan et al. [10] obtained similar metallic dispersion (D_{Ru} = 32.2 %) in a 3% Ru/Al_2O_3 prepared by incipient wetness impregnation of Ru(III) acetylacetonate precursor and performing the calcination treatment under 10 %H_2/Ar flow. As a result, the $RuAl_{IWI}$ catalyst contains a Ru surface area of 0.79 m^2 g^{-1} while that of $RuAl_{GAI}$ is 3.90 m^2 g^{-1}.

In a final step, the catalytic performance of the catalysts was evaluated in order to determine the effect of the preparation method on activity. Fig. 4 shows the CO_2 conversion (above) along with product selectivity (below) as a function of the reaction temperature for Ni/Al_2O_3 and Ru/Al_2O_3 catalysts, respectively. As previously reported [18], Ru-based catalysts were more active than Ni-based ones due to the higher ability of the former to dissociate hydrogen at lower temperature. Thus, the catalytic activity order is as follows: $RuAl_{GAI}$ > $RuAl_{IWI}$ > $NiAl_{GAI}$ > $NiAl_{IWI}$. The activity profiles of Ni/Al_2O_3 samples are not so different, as shown in Fig. 4a. In both cases, the CO_2 conversion (reaction rate) increases exponentially with temperature from 225 °C (onset reaction temperature) to 325 °C and then, this increase slows down as the reagents are depleted and equilibrium conversion is approached. It must be noted that the CO_2 conversion is slightly higher for $NiAl_{GAI}$ catalyst in the studied temperature range, resulting in a T_{50} (temperature at which 50 % of CO_2 conversion is obtained) only 5 °C lower. However, a more significant difference can be observed in selectivity (Fig. 4b): $NiAl_{IWI}$ produces more CO than $NiAl_{GAI}$ catalyst at mild temperatures (T ≈ 300 °C), although never more than 3.5 % of converted CO_2. In fact, the CO selectivity of $NiAl_{IWI}$ at 300 °C is around 2.5 times higher than that of $NiAl_{GAI}$ catalyst (3.2 vs. 1.3 %). The small amount of carbon monoxide is produced either from reverse water gas shift (RWGS) or reforming reactions.

On the other hand, the higher CO_2 conversion and CH_4 selectivity observed for $NiAl_{GAI}$ catalyst are probably related to a higher Ni surface area (8.25 vs. 5.62 m^2 g^{-1}). This hypothesis was supported by calculations of *TOFs* at 250 °C. Note that by definition, TOF assumes that reaction takes place at any point of metal surface. However, under CO_2 methanation conditions, the partial H_2 pressure is at least four times higher than that of CO_2, which disfavors the adsorption of the latter. Consequently, metal particles will be largely covered by H_2. Also, considering that the support (γ-Al_2O_3 in this study) is able to adsorb or active CO_2, it can be assumed that CO_2 methanation takes place at the perimeter of metal-support interface rather than on surface, as reported in a previous work [39]. Therefore, for more realistic comparison, TOF was normalized with respect to interfacial length or perimeter (TOF/I_0, Table 1). The total metal-support perimeter per metal surface area (I_0) was calculated by Eq. (10), which was proposed by Kourtelesis et al. [40] and is based on developments reported by Duprez et al. [41].

$$I_0\left(m_{interface}/m_{Me}^2\right) = \frac{S_{Me}^2 \times \beta \times \rho_{Me} \times AW_{Me}}{N_A \times atA_{Me}} \quad (10)$$

where, S_{Me} is the metallic surface area in m^2 g_{Me}^{-1}, β is a particle shape factor (33.3 for hemispherical particles), ρ_{Me} is the density of the metal in g m^{-3}, AW_{Me} is the metal atomic weight of the metal in g mol^{-1}, N_A is the Avogadro number, and atA_{Me} is the area occupied by a single metal atom ($6.49 \cdot 10^{-20}$ m^2 Ni $atom^{-1}$ and $6.13 \cdot 10^{-20}$ m^2 Ru $atom^{-1}$). It can be observed that TOF/I_0 values are of the same order of magnitude, suggesting that the CO_2 methanation rate per metal atom at the interface for supported catalysts with average Ni particle perimeters of 18.2 nm ($NiAl_{IWI}$ catalyst) and 35.2 nm ($NiAl_{GAI}$ catalyst) is quite similar. Recently, the structure sensitivity of CO_2 methanation over supported metals has been studied by various authors. For instance, Vogt at al. [29] clearly reported structure sensitive CO_2 methanation over Ni/SiO_2 catalysts with small particle sizes ranging from 1 to 6 nm, concluding that the more active Ni atoms are those forming clusters of 2–3 nm. The high *TOF* of these clusters was attributed to an intermediate adsorption strength of CO on Ni, which was reported to be a reaction intermediate of CO_2 methanation on Ni/SiO_2 catalyst. However, Beierlein et al. [14] demonstrated that the specific activity does not depend on Ni particle size within a range from 6 to 91 nm, observing a linear correlation between the activity and Ni surface area and concluding that CO_2 methanation on highly loaded Ni/A_2O_3 catalysts is a structure insensitive reaction. Therefore, it seems that structure sensitivity clearly depends on the range of Ni particle size studied as well as the metal-support combination used. In our case, the results are in agreement with the findings of the second authors, since the observed specific activity barely increase when decreasing particle size from 11 to 6 nm.

Analogously, the light-off and selectivity curves of Ru/Al_2O_3 catalysts are displayed in Fig. 4c and d. In this case, the onset temperature for both samples is 200 °C and the equilibrium CO_2 conversion is reached at the same temperature (X_{CO_2} at 400 °C = 82 %). Nevertheless, the increase in CO_2 conversion with temperature for $RuAl_{GAI}$ is faster than for

Table 2
Physicochemical properties of monometallic Ni and bimetallic catalysts.

Catalyst	Ni cont. (%)[a]	Ru cont. (%)[a]	S_{BET} ($m^2\ g^{-1}$)[b]	Des. H_2 (μmol g^{-1})[c]	D_{Ni} (%)[d]
NiAl	10.8	0	160	67.0	11.5
Ni-0.5RuAl	12.6	0.51	168	89.3	19.4
Ni-1.0RuAl	11.5	1.12	174	125.0	26.3
Ni-1.5RuAl	11.8	1.63	175	151.8	31.1

[a] Determined by ICP.
[b] Calculated by BET equation.
[c] Calculated from H_2-TPD profiles at T < 500 °C.
[d] Estimated from STEM micrographs.

$RuAl_{IWI}$ catalyst, which leads to a notable 20 °C left shift of the light-off curve (i.e., superior activity at low temperature). Regarding the selectivity towards CH_4, it was higher than 99.5 % in the range of studied temperatures and only trace amounts of CO in terms of ppm were detected for $RuAl_{GAI}$ catalyst (Fig. 4d). Considering that metal particles of $RuAl_{GAI}$ are five times smaller than that of $RuAl_{IWI}$ catalyst, one could expect a bigger difference in catalytic performance. This suggests that metal-support interface of the former is less active, as revealed by TOF/I_0 values also summarized in Table 1. Note that TOF/I_0 value is around one order of magnitude lower for $RuAl_{GAI}$ catalyst, suggesting that CO_2 methanation is structure sensitive on RuAl catalysts. Indeed, a lower specific methanation activity on small Ru particles or clusters had already been reported by several authors [8–10]. According to them, CO formation via r-WGS is favoured rather than CO_2 methanation on atomically dispersed or low coordinated small Ru particles. Despite that fact, a considerable T_{50} value gradient of 20 °C is observed, which evidences that a more active catalyst is obtained by GAI method.

3.2. Effect of Ru co-impregnation

Monometallic Ni and Ru catalysts prepared by Glycerol Assisted Impregnation (GAI) achieved better methanation activity compared to those prepared by incipient wet impregnation. In a second step, bimetallic Ni-based catalysts with small Ru contents (< 2 wt%) were prepared following the GAI coimpregnation procedure. The physicochemical properties of $NiAl_{GAI}$ and bimetallic catalysts (Ni-0.5RuAl, Ni-1.0RuAl and Ni1.5RuAl) are shown in Table 2.

As observed, the metal contents determined by ICP are very close to the nominal values, indicating that no relevant amount of metal was lost during the synthesis. Interestingly, the specific surface area slightly increases with Ru content: 5, 9 and 10 %, respectively. This unexpected trend can be explained by analysing the pore size distribution of the catalysts (Fig. S3, supplementary material). The monometallic catalyst ($NiAl_{GAI}$) presents a narrow unimodal mesopore size distribution centered at 7.3 nm, whereas bimetallic catalysts exhibit wider and bimodal distributions with maxima between 6 and 10 nm. As already discussed, $NiAl_{GAI}$ catalyst presents similar particles with sizes probably above 7 nm, which partially or completely block the mesopores of the support. However, the bimodal distribution verified for bimetallic catalysts might be due to the presence of particles with well differentiated size or morphology, which might penetrate into the small pores of γ-Al_2O_3. Ru incorporation widens the distribution but decreases its intensity, which finally results in a slight increase of S_{BET} from 168 to 175 $m^2\ g^{-1}$ and similar pore volume of 0.42 $cm^3\ g^{-1}$. Thus, introduction of Ru makes some improvement in textural properties of Ni/Al_2O_3 catalyst.

XRD analysis was also performed for bimetallic catalysts (not shown). However, no characteristic peaks of both metals were detected (crystallites sizes < 5 nm). This observation is in agreement with N_2 physisorption results and indicates that Ni and Ru are finely dispersed.

Concerning catalysts' resistance against oxidation, $NiAl_{GAI}$ and Ni-1.0RuAl samples were exposed to three consecutive RedOx cycles at 325 °C. Each RedOx cycle consisted of feeding 15 oxidative pulses (5 cm^3 of 5%O_2/He) followed by another 15 reductive pulses (5 cm^3 of 5% H_2/Ar). On that way, the effect of O_2, fed in a concentration similar to that typically presented in flue gases, on the catalysts was estimated and their reversibility was determined. Note that the resistance to oxidation of $3RuAl_{GAI}$ catalyst was measured at 550 °C in order to ensure that its oxidation was effective. The reversibility values of $NiAl_{GAI}$ and Ni-1.0RuAl catalysts, defined as the percentage of Ni reduced per cycle after sample being exposed to 15 oxidative pulses (Eq. 2), are shown in Fig. 5.

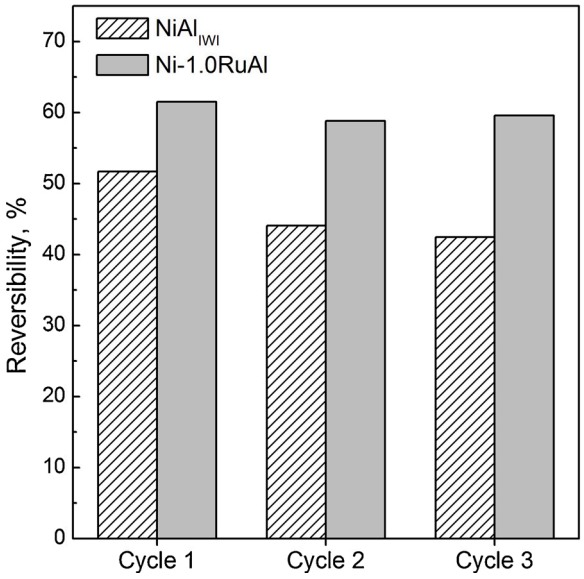

Fig. 5. Resistance against oxidation, expressed as reversibility, of $NiAl_{GAI}$ and Ni-1.0RuAl catalysts for 3 consecutive RedOx cycles at 325 °C.

It can be clearly observed that the reversibility values of the bimetallic catalyst are superior to those of monometallic one in all cycles, observing the major difference in the third cycle: 60 vs. 42 %, respectively. This indicates that incorporation of Ru provides higher resistance to oxidation and/or higher capacity to recover the reductive state than the monometallic $NiAl_{GAI}$. The observed higher reversibility is due to ruthenium role as promotor of nickel reduction in the bimetallic catalyst, i.e., H_2 is firstly dissociated on Ru surface and then can migrate to neighbouring NiO particles facilitating their reduction [23]. Furthermore, it can be noticed that the reversibility of monometallic catalysts decreases from 52 % (cycle 1) to 42 % (cycle 3), while that of bimetallic catalyst remain stable around 60 %. Although the decrease from second to third cycle is not so pronounced (- 2%), it seems that the reversibility value of $NiAl_{GAI}$ sample could keep decreasing in further consecutive cycles due to a progressive formation of NiO that is no longer able to be reduced by remaining Ni°. The fact that reversibility of bimetallic system is apparently stable, suggests that Ni particles are near to and surrounded by Ru ones, which avoids or at least slows down the formation of non-reversible NiO particles. However, as reported by Rynkowski et al. [19], the presence of Ru does not prevent the formation of spinel

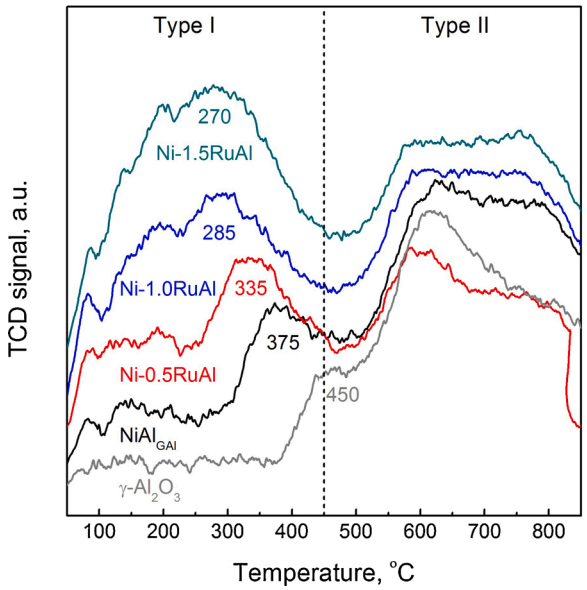

Fig. 6. H_2-TPD profiles of γ-Al_2O_3 support, monometallic Ni and bimetallic catalysts.

type oxides at long term and high temperatures. Finally, it must be highlighted that the H_2 uptake was around 2 times the O_2 uptake at 550 °C for $RuAl_{GAI}$ catalyst, suggesting, as expected, 100 % reversibility.

On the other hand, the hydrogen adsorption capacity was determined by TPD. Thus, H_2-TPD profiles of the samples are depicted in Fig. 6.

It can be observed that all profiles exhibited two bands, before and after 450 °C. While the band below 450 °C can be generally attributed to H_2 chemisorbed on metal particles (type I), the one at higher temperature is associated with H_2 desorption from the subsurface alumina layers or with the spillover phenomenon (type II) [42]. Indeed, the H_2-TPD profile of bare γ-Al_2O_3 does not show any signal variation below 400 °C but an intense band at higher temperature, which might be related to a dehydroxylation process (Fig. 6). Likewise, the band at low temperatures can be divided into several peaks. For instance, the monometallic $NiAl_{GAI}$ catalyst, presents a main peak at 375 °C and additional H_2 desorption below 250 °C. According to Ewald et al. [4], the main peak corresponds to hydrogen chemisorbed on Ni surface while the TCD signal at low temperatures can be ascribed to hydrogen adsorbed on the corners of large Ni particles or on better dispersed particles. Noteworthy, the main peak position shifts towards lower temperatures and its intensity increases with Ru content, suggesting that the amount of exposed Ni atoms grows accordingly. Such increase in Ni dispersion was also reported by other authors who incorporated Ru [26], Cr [12] or Fe [21]. The amounts of desorbed H_2 calculated from TPD profiles integration are summarized in Table 2. Note that this parameter duplicates with co-impregnation of 1.5 % Ru on Ni/Al_2O_3 formulation, i.e., the fraction of exposed metal notably rises. Accordingly, the ability to supply dissociated hydrogen under methanation reaction conditions remarkably increases with the Ru content. Based on H_2 desorption data, Ni dispersion on the monometallic catalyst was also estimated, resulting a value of 7.9 % (11.5 % by TEM, Table 1). In the case of bimetallic catalysts, dispersion cannot be estimated since exposed atoms of both Ni and Ru, in major and minor extent respectively, contribute in the total H_2 desorption below 450 °C. Anyway, the amount of desorbed hydrogen compared to that of $NiAl_{GAI}$ catalyst is more than twice for Ni-1.5RuAl catalyst and hence, this suggests that its metal surface could be around double.

In order to determine the morphology, size and distribution of the supported bimetallic particles, HAADF-STEM analysis was conducted. The high-angle Z-contrast annular field imaging together with EDX

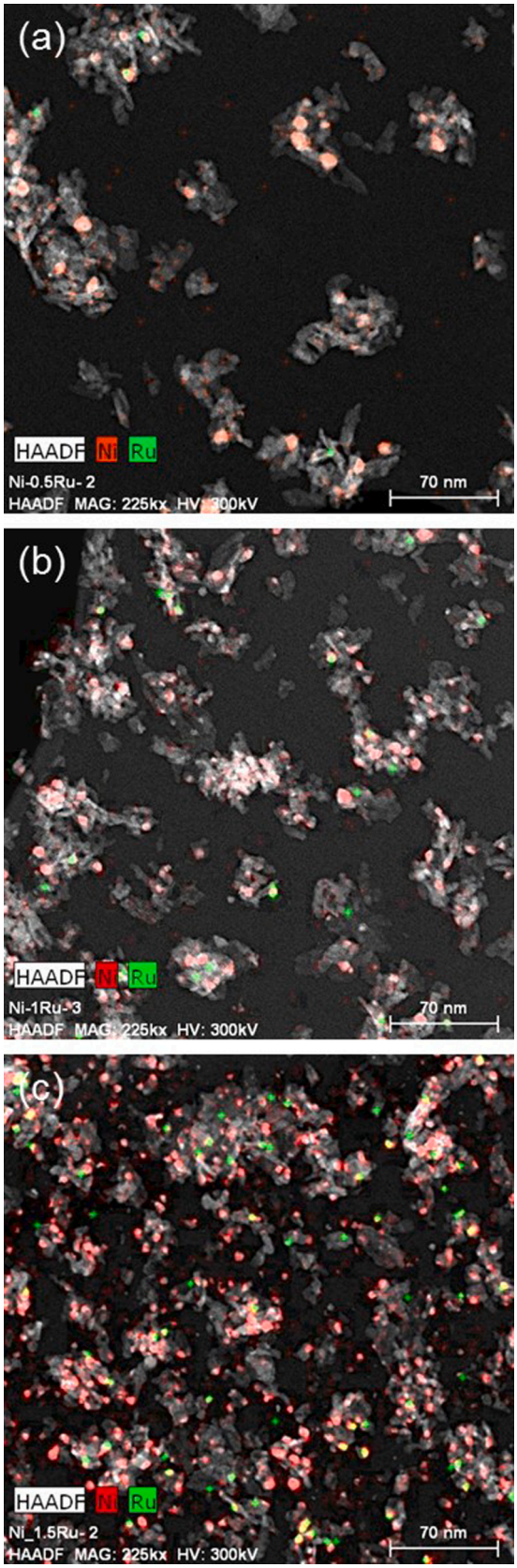

Fig. 7. STEM micrographs with respective EDX maps for (a) Ni-0.5RuAl, (b) Ni-1.0RuAl and (c) Ni-1.5RuAl catalysts.

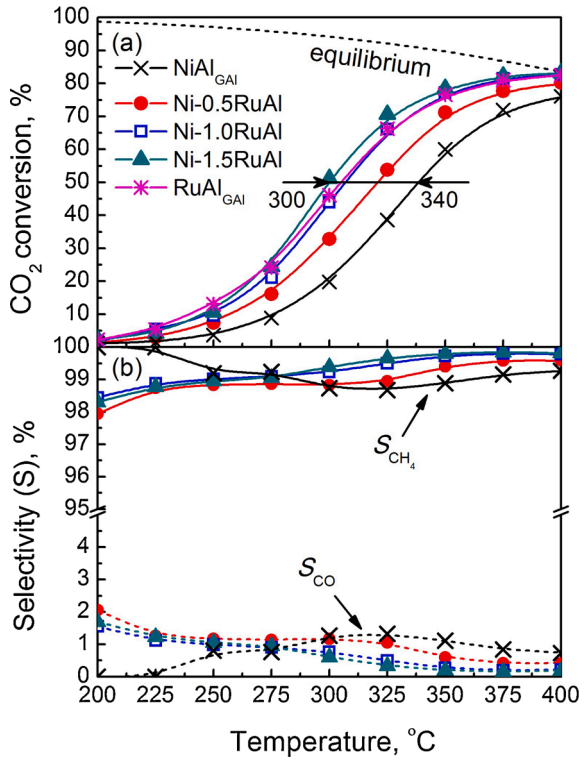

Fig. 8. (a) Light-off curves together with (b) products (CH_4 and CO) selectivity profiles of monometallic and bimetallic catalysts. Reaction conditions: P =1 bar, H_2: CO_2 ratio = 4 and WHSV = 30,000 mL h^{-1} g_{cat}^{-1}.

mapping allowed us differentiating between two or more elements, such as Al (Z = 13), Ni (Z = 28) and Ru (Z = 44). STEM micrographs together with EDX maps of bimetallic catalysts are shown in Fig. 7. It can be observed that Ni (red coloured) and Ru (green coloured) are homogenously dispersed as individual spherical particles, which means that no alloy is formed during the calcination at 550 °C [26]. Noteworthy, the Ni-0.5RuAl catalyst presents an average Ni particle size of 7.4 nm (calculated from around 50 particles), 4 nm lower than that obtained for monometallic NiAl$_{GAI}$ catalyst. This parameter is even lower for Ni-1.0RuAl and Ni-1.5RuAl, with values of 6.3 and 5.9 nm, respectively. Therefore, Ni particle size is lowered by increasing the amount of co-impregnated Ru. Regardless the metal loading (0.5, 1.0 or 1.5 %), the Ru particle size resulted to be around 4−5 nm for all bimetallic catalysts. Note that some of these particles are located near to Ni ones, especially for catalysts with higher Ru contents (see Fig. 7b and c). The fact that Ni and Ru particles are next to each other or in intimate contact is in agreement with the enhanced reducibility observed by H_2-TPR: the neighbour Ru particle acts as H supplier via spillover mechanism favouring the reduction of Ni^{2+} [23].

As is in the case of monometallic catalysts, Ni dispersion on bimetallic catalysts was also estimated by d-FE model and the results are summarized in Table 2. As already observed by H_2-TPD, the Ni dispersion is significantly enhanced with Ru loading. In fact, Ni dispersion increases 9.4, 15.6 and 20.0 % by adding 0.5, 1.0 and 1.5 % of Ru, respectively. This behaviour might indicate that both Ru and glycerol solvent act as structural promoters during the calcination process, avoiding the excessive growing or sintering of Ni. Based on the characterization results properly discussed above, it is expected that Ni/Al_2O_3 catalysts performances are improved with the incorporation of small percentage of Ru in the formulation.

Thus, once bimetallic catalysts were characterized and the effect of Ru on physicochemical properties of Ni/Al_2O_3 determined, their catalytic performance was studied. The conversion-temperature as well as the selectivity-temperature curves of bimetallic catalysts are shown in Fig. 8. For comparison purposes, the light-off curves obtained for NiAl$_{GAI}$ and RuAl$_{GAI}$ catalysts are also displayed. It can be clearly observed that the addition of increasing amounts of co-impregnated Ru leads to a notable increase of the sigmoid curve slope, especially at mild temperatures (from 275 to 325 °C). Accordingly, the T_{50} value is lowered 40 °C by only co-impregnating 1.5 %Ru, which indicates that the presence of Ru considerably improves the activity of Ni/Al_2O_3 formulation. Although different trends are observed depending on the temperature, all catalysts exhibit selectivity to CH_4 higher than 98.5 %. The slightly lower S_{CH_4} (or higher CO production) observed for bimetallic catalysts at low temperature compared to that of NiAl$_{GAI}$ catalyst may be related to some desorption of CO from low coordinated and inactive Ni and Ru particles. Even so, the methane yield clearly increases with Ru content, being the productivity order at 300 °C as follows: Ni-1.5RuAl (Y_{CH_4} = 51

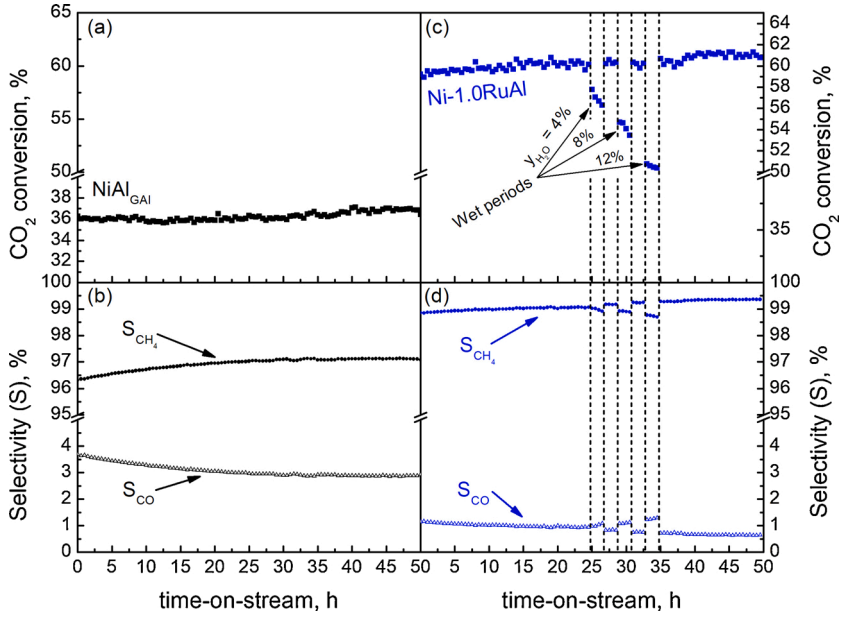

Fig. 9. Evolution of CO_2 conversion and CH_4/CO selectivity with time-on-stream over 50 h for (a, b) NiAl$_{GAI}$ and (c, d) Ni-1.0RuAl catalysts. Reaction conditions: T = 325 °C, P =1 bar, H_2: CO_2 ratio = 3 and WHSV = 30,000 mL h^{-1} g_{cat}^{-1}. Stability test of Ni-1.0RuAl catalyst includes 3 wet periods of 2 h at y_{H_2O} = 4, 8 and 12 %.

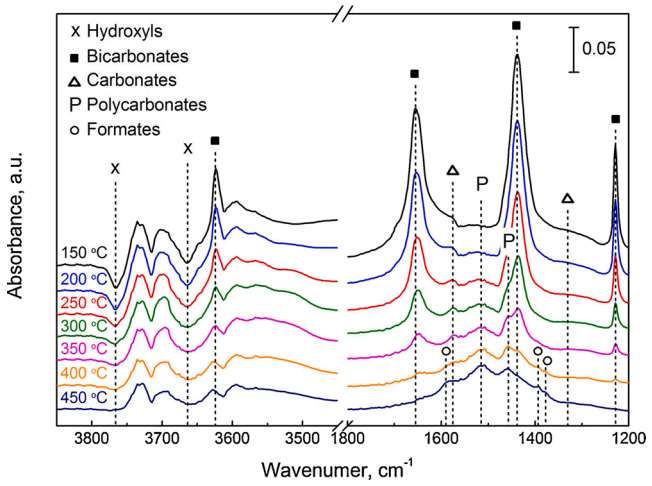

Fig. 10. FTIR spectra collected during CO_2 adsorption (5% CO_2/Ar) over bare γ-Al_2O_3.

%) > Ni-1.0RuAl (Y_{CH_4} = 44 %) > Ni-0.5RuAl (Y_{CH_4} = 32 %) > $NiAl_{GAI}$ (Y_{CH_4} = 20 %). It should be noted that Ni-1.0RuAl catalyst (T_{50} = 305 °C) shows almost the same activity as $3RuAl_{GAI}$ catalyst, whose noble metal content is three times higher.

According to the characterization results, co-impregnation of Ru increases Ni dispersion. Besides, the presence of small Ru particles close to Ni ones considerably improves reducibility and hydrogen chemisorption capacity of nickel. Under reaction conditions, this leads to a greater amount of dissociated H_2, which is an essential reaction intermediate, and hence to a superior activity. Thus, the great enhancement observed in the catalytic performance can be attributed to a synergistic effect between Ni and Ru, as also reported by Liu et al. [26].

The catalytic behaviour of alumina supported Ni and Ru catalysts proved to be stable for 24-h-on stream and at stoichiometric feed ratio in the former work [34]. Then, in order to accelerate the aging of the catalyst, the stability of monometallic $NiAl_{GAI}$ and bimetallic Ni-1.0RuAl catalyst was evaluated for 50 h-on-stream under harsher reaction conditions: at 325 °C (far for equilibrium conversion) and under sub-stoichiometric feed ratio (H_2/CO_2 = 3). Noteworthy, the activity of $NiAl_{GAI}$ catalyst resulted to be stable during the evaluated period, observing CO_2 conversion values within 35 and 37 %, as shown in Fig. 9a. This indicates that the catalyst did not suffer from any type of deactivation such as particle sintering or poisoning [4] even though more CO was produced (Y_{CO} = 1.33 %) as consequence of sub-stoichiometric feed. Besides, the CH_4 selectivity also remained stable, observing values within 96.3 and 97.1 %.

In the case of the bimetallic catalyst, the stability test also included three wet periods (t =2 h) in which increasing amounts of water (10, 20 and 30 mL/min) were fed interspersed by dry periods. It can be observed that, before 25 h-on-stream, the catalytic performance remained stable as observed for $NiAl_{GAI}$ catalyst, obtaining CO_2 conversion and CH_4 selectivity average values of 60 and 99 %. However, the feed of increasing amounts of water, led to a CO_2 conversion drop of around 3 (y_{H_2O} = 0.04), 6 (y_{H_2O} = 0.08) and 9% (y_{H_2O} = 0.12) without a remarkable CH_4 selectivity decrease (0.1, 0.25 and 0.5 %). This behavior indicates that water is strongly adsorbed on part of active sites, temporally rendering them unavailable for the reaction. Nevertheless, the activity was completely recovered when switching to dry conditions, indicating that water adsorption or inhibition effect is reversible at short term. Thus, based on the above activity and stability results, it can be concluded that glycerol assisted impregnation is a viable catalyst preparation method.

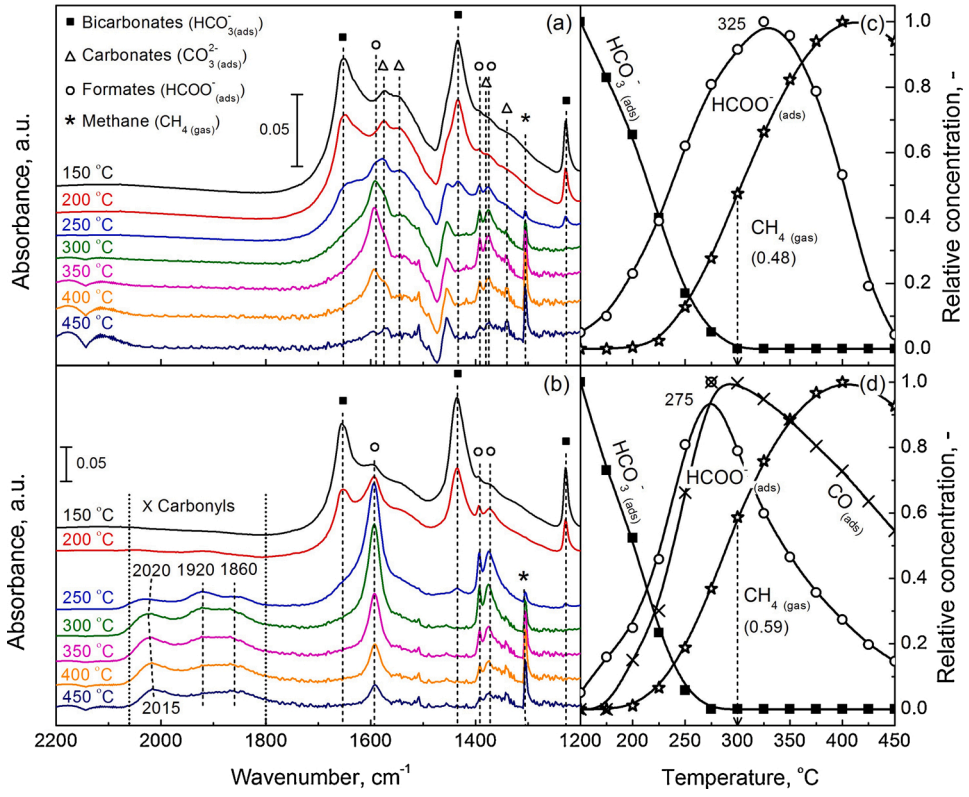

Fig. 11. FTIR spectra recorded at different temperatures under CO_2 methanation conditions (Feed = 5% CO_2/20 % H_2/Ar) along with the corresponding C-species evolution of (a, c) $NiAl_{IWI}$, and (b, d) $NiAl_{GAI}$ catalysts.

3.3. Operando FTIR measurements

Although it has been shown that bimetallic catalyst have enhanced catalytic properties based on characterization as well as activity results, the individual roles of both Ni and Ru on the CO_2 methanation reaction mechanism are not clear yet. Such roles, as well as the identification of the reaction intermediates, will be analysed in this section by *Operando* FTIR study. Fig. 10 shows the evolution of CO_2 adsorption FTIR spectra with temperature for bare γ-Al_2O_3. Immediately after 5%CO_2/Ar exposure at 150 °C (see black spectrum), three clearly distinguishable bands appeared at 1653, 1437 and 1228 cm^{-1}, whose intensity grows with time up to 30 min. These bands, already identified by many authors in the literature [9,43–46], correspond to asymmetric as well as symmetric O—C—O stretching ($\nu_{a(OCO)}$ and $\nu_{s(OCO)}$) and OH deformation ($\delta_{(OH)}$) vibration modes of bicarbonate species, respectively. Besides, two negative bands can be observed in the hydroxyl region (3800−3600 cm^{-1}) at 3765 and 3665 cm^{-1} together with a narrow positive peak at 3620 cm^{-1}. The negative ones are attributed to the vibration of OH– groups adsorbed along alumina surface whereas the positive one corresponds to $\nu_{(OH)}$ vibration mode of bicarbonates. The presence of negative bands clearly indicates that bicarbonates are formed from CO_2 chemisorption on OH– groups of γ-Al_2O_3, which are partially consumed after 30 min CO_2 adsorption [43]. Additionally, other wide and weak bands appear at 1575 and ≈ 1330 cm^{-1}, which might be assigned to $\nu_{a(OCO)}$ and $\nu_{s(OCO)}$ vibration modes of (chelating) bidentate carbonates. It is expected that carbonates are formed from CO_2 chemisorption on surface O^{2-} of γ-Al_2O_3 acting as Lewis basic sites [44].

The intensity of bicarbonate bands along with those of bidentate carbonates progressively decreases with temperature until practically disappearing at 400 °C, indicating that these species are not strongly attached to alumina. In fact, the weak-medium bond strength of bicarbonate has already been observed by CO_2-TPD [34,47]. However, the increase of temperature gives rise to small bands at 1515 and 1457 cm^{-1}, which might be related to formation of more stable organic compounds. Furthermore, additional discrete bands are observed at 1393 and 1375 cm^{-1}, suggesting the presence of formate species. The formation of formates on alumina have already been reported and we suggest they come from reaction between bicarbonate or carbonate and residual H chemisorbed during the pre-treatment [9].

After studying CO_2 adsorption over the bare support, the CO_2 methanation was analysed by means of *Operando* FTIR over monometallic Ni formulations ($NiAl_{IWI}$ and $NiAl_{GAI}$ catalysts). FTIR spectra recorded under reaction conditions from 150 to 450 °C along with their respective C-species evolution for $NiAl_{IWI}$ and $NiAl_{GAI}$ catalysts are shown in Fig. 11. Starting by the analysis of $NiAl_{IWI}$ catalyst results (Fig. 11a), note that the black spectrum, which was recorded at 150 °C after 30 min under reaction stream exposure, shows more intense bands in the carbonate region (1800-1200 cm^{-1}) than bare alumina (Fig. 9). Specifically, the bands assigned to bidentate carbonates at 1574 and 1330 cm^{-1} overlap with additional new ones at 1545 and 1380 cm^{-1}, which might be assigned to vibration of monodentate carbonates [3,45]. This greater number of surface carbonates could be associated with the presence of non-reducible $Ni^{2+}O^{2-}$ or even $NiAl_2O_4$ able to adsorb CO_2 [37]. As the temperature increases, these bands disappear giving rise to clear and intense bands at 1595, 1395 and 1375 cm^{-1}, characteristic of 3 vibration modes of formates: asymmetric OCO stretching ($\nu_{a(OCO)}$), CH deformation ($\delta_{(CH)}$) and symmetric OCO stretching ($\nu_{s(OCO)}$), respectively [9,31,47]. Complementary, the band corresponding to CH stretching ($\nu_{(CH)}$) is observed at 2900 cm^{-1} (not shown), confirming the formation of formate species. After that, new increasing bands appear at 3016 cm^{-1} ($\nu_{a(CH)}$) and 1305 cm^{-1} ($\delta_{(CH)}$), indicating the formation of methane gas [33]. Note that no bands were verified in the carbonyl region (2100−1800 cm^{-1}) but the characteristic bands of CO gas were observed at 2175 and 2105 cm^{-1}, suggesting that no detectable amount of CO_{ads} could have formed on Ni° by CO_2 disproportionation.

Analogously, Fig. 11b displays FTIR spectra of $NiAl_{GAI}$ catalyst. As expected, the same bands and/or species were identified in the carbonate region but with different concentration. In fact, the bands corresponding to carbonates are less intense at the starting temperature (150 °C) probably due to the absence of NiO or $NiAl_2O_4$ acting as basic sites in the catalyst prepared by GAI method. Notably, unlike $NiAl_{IWI}$, $NiAl_{GAI}$ catalyst presents 3 bands in the carbonyl region (2100−1800 cm^{-1}) located at 2020, 1920 and 1860 cm^{-1}. The first is ascribed to the stretching vibration of terminally or linearly adsorbed CO on top single Ni atoms, whereas the other two can be attributed to weakly and strongly attached bridged carbonyls on neighbouring Ni atoms, respectively [20,29,48]. Interestingly, the band corresponding to linearly adsorbed CO shifts with temperature, while the others remain at the same frequency. This shift is associated with changes in CO covering on Ni surface and suggests that these CO species participate in the CO_2 methanation mechanism. On the contrary, bridged carbonyls are more stable and may not react with hydrogen [29]. Furthermore, it is wide known that the $\nu_{(CO)}$ frequency (in wavenumbers) is associated with the metallic dispersion: the higher the frequency, the higher the dispersion or the lower the Ni particle size. Thus, according to the 3 $\nu_{(CO)}$ bands, $NiAl_{GAI}$ catalyst presents particles with different sizes indicative of highly, moderately and poorly dispersed Ni° [48]. This observation is consistent with TEM results, according to which a particle size distribution ranging from 3 to 20 nm is observed. Noteworthy, the lack of adsorbed carbonyls on the catalyst prepared by IWI suggests that there are differences in the Ni electronic state when comparing Al_2O_3 supported Ni catalysts. In the case of $NiAl_{IWI}$, it seems that Ni, after reduction pretreatment, is partially oxidized or positively charged ($Ni\delta^+$) due to the interaction with remaining non reducible Ni^{2+} species or with Al^{3+} cations exposed on the alumina surface. As the exposed Ni has electron deficiency, $NiAl_{IWI}$ presents lower affinity to dissociate CO_2 by H-assistance or adsorb CO and, hence, no bands are detectable within 2100−2000 cm^{-1}. Although Ni^{2+} is also able to adsorb CO, no bands were observed among 2300 and 2100 cm^{-1} assignable to CO on Ni^{2+} sites. $NiAl_{GAI}$, by contrast, has much more affinity to CO adsorption since all nickel is in reduced state (Ni°) after being calcined under reductive atmosphere (GAI method).

The evolution of the main reaction intermediates and methane with temperature is clearly shown in the attached figures (Fig. 11c and d). In the case of $NiAl_{IWI}$ catalyst (Fig. 11c), it can be observed that the relative concentration of bicarbonates decreases as that of formates increases, following a symmetric evolution (T < 250 °C). This suggests that formates mainly arise from bicarbonates although it cannot be excluded that, in minor extent, carbonates are also reduced into formates [47]. After that, from 250 °C to 325 °C, adsorbed bicarbonates disappear and the formation rate of formates slows down up to zero, i.e., its relative concentration reaches a maximum. This slowdown or depletion matches with methane appearance, whose relative concentration increases exponentially in agreement with activity results. Finally, at higher temperatures (T > 350 °C), the relative concentration of formates decreases, while that of methane slowly increases up to 425 °C approaching to the limited thermodynamic equilibrium of an exothermal reaction. Thus, it can be assumed that formates at the metal-support interface could participate in methane formation. However, it cannot be claimed that formates are directly hydrogenated following the associative mechanism, since not bands characteristic of methoxy species (reaction intermediates) or methanol have been detected by FTIR, as reported by Solis-García et al. [28]. Finally, the appearance of CO_{gas} from 300 °C together with the absence of adsorbed carbonyls indicates that this by-product could be formed from decomposition of formates as follows:

$$HCOO_{(ads)} \rightarrow HCO_{(ads)} + O_{(ads)} \rightarrow CO_{(ads)} + OH_{(ads)} \rightarrow CO_{(gas)} + H_2O_{(gas)} \quad (11)$$

On the other hand, the corresponding species evolution of $NiAl_{GAI}$ sample is displayed in Fig. 11d. Note that, in general, the relative

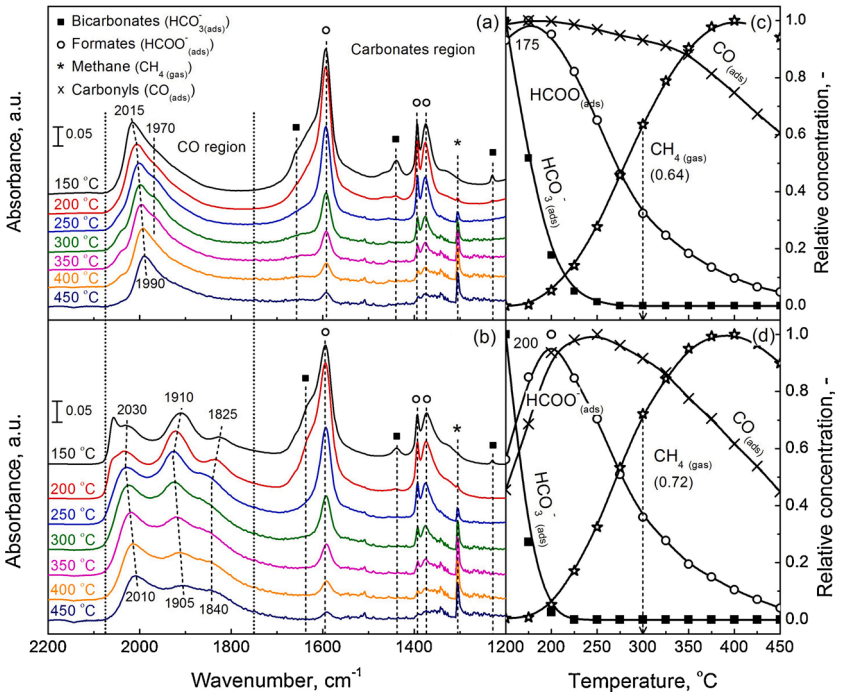

Fig. 12. FTIR spectra recorded at different temperatures under CO_2 methanation conditions (Feed = 5% CO_2/20 % H_2/Ar) along with the corresponding C-species evolution of (a, c) $RuAl_{GAI}$ and (b, d) Ni-1.0RuAl catalysts.

concentration curves for adsorbed species follow the same trend but are clearly shifted towards lower temperatures. In fact, bicarbonates are depleted or transformed into formates faster (at 275 °C) and the maximum of formates concentration curve, which is also volcano-shaped, is clearly shifted 50 °C into the left (275 vs. 325 °C). Carbonyls relative concentration, in turn, increases with temperature up to 300 °C and then starts depleting. We suggest that carbonyls, which appear from 200 °C, might arise from formates decomposition (Eq. (11)) or, less probably, from CO_2 dissociative adsorption. Wang et al. [9] also studied CO_2 methanation by FTIR on a 5%Ru/Al_2O_3 catalyst and concluded that formates are reactive towards the formation of adsorbed CO when it is close to metal particles. From 225 °C, the linearly bonded and, in minor extent, weakly attached bridged carbonyls may be hydrogenated into methane, whereas the strongly attached bridged ones remain stable. From 300 °C, some of the bridged carbonyls could be desorbed as CO_{gas}, as revealed by bands at 2175 and 2105 cm^{-1}. Noteworthy, the general shift of adsorbed species evolution indicate that $NiAl_{GAI}$ catalyst has a greater capacity to dissociate H_2 and provide H, which is essential to carry out the successive steps of reaction mechanism. This leads to a higher activity at mild temperatures, as evidenced by the higher CH_4 relative concentration of $NiAl_{GAI}$ catalyst at 300 °C (0.59 vs. 0.48).

The FTIR spectra as well as evolution with temperature of adsorbed species over $RuAl_{GAI}$ and Ni-1.0RuAl catalyst are shown in and Fig. 12. Additionally, CO_2 methanation FTIR spectra of $RuAl_{IWI}$ catalyst are included in Fig. S4 (supplementary material). Mainly, the same species as in the case of Ni catalysts are observed in carbonate region with similar evolution. However, the position and intensity of bands appearing at carbonyl region are different, i.e., the type and distribution of carbonyl species are not the same. In fact, FTIR spectra of Ru/Al_2O_3 catalysts show a main band at 2015 cm^{-1} at 150 °C that can be attributed to vibration of linearly adsorbed CO over reduced Ru atoms (Ru-CO) [10,31,49]. This band is more intense to that observed for $NiAl_{GAI}$ catalyst, indicating that Ru has a major capacity or more affinity to adsorb CO than Ni. However, unlike $RuAl_{IWI}$ catalyst, $RuAl_{GAI}$ presents a shoulder at 1970 cm^{-1} (Fig. 12a) related to stretching vibration of terminal CO species located at metal-support interface ((Al_2O_3)Ru-CO) [49]. Note that the main band on both Ru catalysts red shifts with temperature from 2015 to 1990 cm^{-1} due to a decrease in Ru surface coverage by CO, whereas the position of the shoulder observed for $RuAl_{GAI}$ catalyst does not shift and it vanishes above 350 °C along with appearance of CO gas in the cell. Based on these observations, it can be concluded that on-top CO species participates in the reaction but the same cannot be stated for CO species adsorbed at the interface. It seems that this species may not participate in the reaction but eventually desorbed, indicating that $RuAl_{GAI}$ presents a higher fraction of inactive Ru atoms in agreement with the lower TOF/I_0 value obtained.

In the case of the bimetallic catalyst, it should be considered that bands appearing at 2100-1800 cm^{-1} region correspond to carbonyl species adsorbed on both Ni and Ru particles. Thus, what Fig. 12b shows is a combination of bands previously observed for $NiAl_{GAI}$ and $RuAl_{GAI}$ catalysts, characteristic of above-mentioned CO species. The difference is that a new peak is observed at 2056 cm^{-1} attributed to geminal dicarbonyls on low coordinated Ru [9,10,49], which disappear above 250 °C. According to Panagiotopoulou et al. [50], this species disappears with temperature since it is converted into linearly adsorbed CO due to H_2-induced agglomeration of low coordination Ru sites into bigger Ru clusters. Noteworthy, the combination band at 2030 cm^{-1} corresponding to linearly adsorbed carbonyls is significantly more intense than on $NiAl_{GAI}$ catalyst, indicating that CO adsorption is promoted by the co-impregnation of 1% Ru. On the other hand, the band corresponding to weakly attached bridged carbonyls (at 1910 cm^{-1}) is clearly more intense compared to that observed on $NiAl_{GAI}$ catalyst, which confirms that the bimetallic catalyst presents a higher Ni dispersion (26.3 vs. 11.5 % according to TEM results). As the temperature increases, bands at 2030 and 1910 cm^{-1} first blue shift up to 250 °C and then red shift to 2010 cm^{-1} and 1905 cm^{-1}, respectively. The red shift matches with the appearance of CH_4 band at 1305 cm^{-1}, suggesting that both species could be reaction intermediates.

Regarding to C-species evolutions of $RuAl_{GAI}$ and Ni-1.0RuAl catalysts (Fig. 12c and d), it can be seen that they are quite similar (except to that of CO), observing a shift of curves towards lower temperatures with respect to those of monometallic Ni catalysts. The shift is due to an enhanced catalytic activity, as demonstrated by H_2-TPD runs. In fact, the

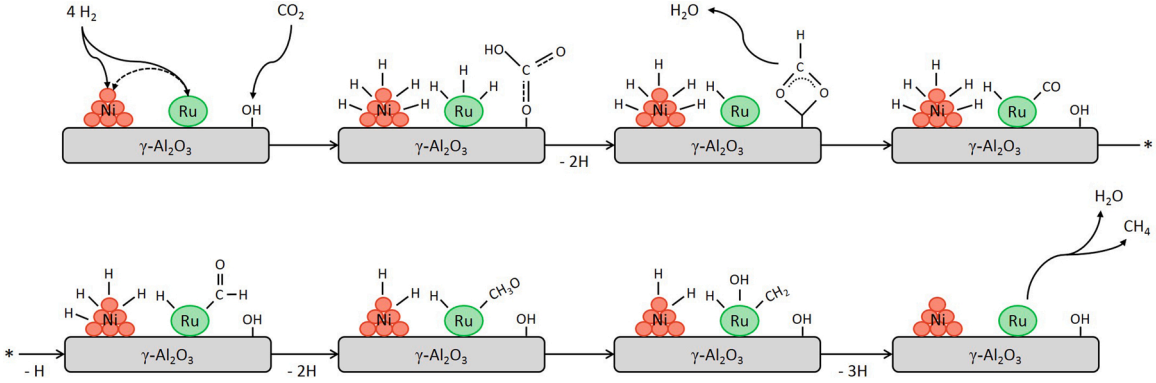

Scheme 1. CO_2 methanation reaction pathway proposed on Ni-1.0RuAl catalyst.

bands corresponding to bicarbonate species vibration at 150 °C are much less intense than those observed for $NiAl_{GAI}$ catalyst in both cases, suggesting that bicarbonates are more easily hydrogenated into formates, which reach maximum concentration value at 175 and 200 °C, respectively. After that, formates at the interface are decomposed into carbonyls and, subsequently, part of carbonyls (most probably linear carbonyls) are hydrogenated into CH_4, which relative concentration at 300 °C is 0.64 (for $RuAl_{GAI}$) and 0.72 (for Ni-1.0RuAl).

Finally, it should be highlighted that $RuAl_{GAI}$ presents a considerable higher amount of potentially reactive carbonyls (linearly bonded) but a CH_4 yield similar to that of bimetallic Ni-1.0RuAl catalyst, as can be deduced by comparing its respective spectra and C-species evolution at different temperatures. This suggests that the fraction of carbonyls effectively converted into CH_4 is lower in the monometallic catalyst. In fact, although Ni-1.0RuAl adsorbs less CO, it disposes of an enhanced dissociated hydrogen supply to reduce CO as a result of the Ni-Ru synergetic interaction. Based on these results, it can be concluded that an effective CH_4 formation not only depends on the type and number of adsorbed carbonyls but also on the availability of adjacent H atoms to carry out the C—O bond hydrogenation.

To sum up, Scheme 1 proposes and depicts the proposed reaction pathways on bimetallic Ni-1.0RuAl catalyst deduced from *operando* FTIR results shown in this section.

Firstly, CO_2 is mainly adsorbed on hydroxyl groups (OH^-) of γ-Al_2O_3 to give monodentate bicarbonates (HCO_3^-), whereas H_2 is dissociated and adsorbed on metal surface. After that, dissociated H_2 (H atoms) spillovers and reacts with bicarbonates close to metal particles yielding bidentate formates ($HCOO^-$), which are considered potential reaction intermediates in alumina supported catalysts. Specifically, formates adsorbed at the interface are decomposed into hydroxyls (OH^-) on γ-Al_2O_3 support and carbonyls (CO), which, in the case of monometallic catalysts, are adsorbed either on Ni or Ru surface. However, in the bimetallic system, CO is expected to preferentially adsorb over Ru nanoparticles due to a higher affinity, whereas H_2 is adsorbed on neighboring Ni particles acting as H atoms reservoir. Then, carbonyls are reduced by adjacent H atoms into formyl (COH, not observed), which are subsequently hydrogenated into CH_xO species (hydroxycarbene (CH_2O) or hydroxymethyl (CH_2OH)). At certain hydrogenation degree (x = 1–3), the CO bond cleavage of CH_xO species occurs (rate determining step), finally releasing CH_4 and H_2 molecules [16,31,51].

4. Conclusions

In this work, the low temperature activity of Ni/Al_2O_3 formulation is systematically improved through the use of efficient synthesis (IWI vs. GAI) and the addition of Ru. Overall, catalysts prepared by GAI method presented better catalytic performance than those prepared by IWI. In the case of Ni catalysts, the formation of Ni^{2+} strongly interacting with the support was avoided by GAI synthesis route, resulting in a higher Ni surface area available for the reaction. Instead, GAI method led to a notable increase in the metal dispersion on $RuAl_{GAI}$ catalyst due to the glycerol enclosing effect but, in return, the specific activity (TOF/I_0) of Ru nanoparticles resulted to be two order of magnitude lower since reaction is structure sensitive. On the other hand, the activity of Ni/Al_2O_3 was improved even more by co-impregnation of small amounts of Ru as a result of a synergistic combination. In fact, the bimetallic Ni-1.0RuAl catalyst showed remarkably higher Ni dispersion, reducibility, and CO adsorption capacity than $NiAl_{GAI}$ catalyst, observing a methane yield equal to that of $3RuAl_{GAI}$. Operando FTIR experiments revealed that CO_2 methanation over alumina supported Ni and Ru catalysts proceeds via formation of carbonyl species mainly arising from intermediate formates decomposition, followed by its hydrogenation into CH_4. In the bimetallic system, the potentially most reactive species is CO linearly adsorbed over Ru, which is more easily hydrogenated by H atoms supplied from adjacent Ni particles. We conclude that the enhanced CO_2 methanation activity of bimetallic catalyst is not only due to a promoted CO adsorption but also to a higher supply of dissociated H_2.

Author contributions

Adrián Quindimil: Methodology, Investigation, Data curation, Writing - Original Draft, Visualization.

M. Carmen Bacariza: Methodology, Investigation, Data curation, Writing - Review & Editing, Visualization.

José A. González-Marcos: Verification, Resources, Data curation, Writing - Review & Editing, Visualization.

Carlos Henriques: Conceptualization, Resources, Funding acquisition, Validation, Supervision.

Juan R. González-Velasco: Conceptualization, Resources, Funding acquisition, Validation, Supervision, Project administration.

Declaration of Competing Interest

The authors report no declarations of interest.

Acknowledgments

The support from the Economy and Competitiveness Spanish Ministry (PID2019-105960B-C21), the Basque Government (IT1297-19) and the SGIker (Analytical Services) at the University of the Basque Country are acknowledged. One of the authors (AQ) also acknowledges University of the Basque Country by his PhD grant (PIF-15/351).

Appendix A. Supplementary data

Supplementary material related to this article can be found, in the online version, at doi:https://doi.org/10.1016/j.apcatb.2021.120322.

References

[1] IEA, Global Energy Review 2020, IEA, Paris, 2020. https://www.iea.org/reports/global-energy-review-2020.

[2] IEA, Sustainable Recovery, IEA, Paris, 2020. https://www.iea.org/reports/sustainable-recovery.

[3] T. Burger, F. Koschany, O. Thomys, K. Köhler, O. Hinrichsen, CO_2 methanation over Fe- and Mn-promoted co-precipitated Ni-Al catalysts: synthesis, characterization and catalysis study, Appl. Catal. A Gen. 558 (2018) 44–54.

[4] S. Ewald, M. Kolbeck, T. Kratky, M. Wolf, O. Hinrichsen, On the deactivation of Ni-Al catalysts in CO_2 methanation, Appl. Catal. A Gen. 570 (2019) 376–386.

[5] J. Zhao, Y. Liu, M. Fan, L. Yuan, X. Zou, From solid-state metal alkoxides to nanostructured oxides: a precursor-directed synthetic route to functional inorganic materials, Inorg. Chem. Front. 2 (2015) 198–212.

[6] I. Favier, D. Pla, M. Gómez, Metal-based nanoparticles dispersed in glycerol: an efficient approach for catalysis, Catal. Today 310 (2018) 98–106.

[7] J. Liu, C. Li, F. Wang, S. He, H. Chen, Y. Zhao, M. Wei, D.G. Evans, X. Duan, Enhanced low-temperature activity of CO_2 methanation over highly-dispersed Ni/TiO_2 catalyst, Catal. Sci. Technol. 3 (2013) 2627–2633.

[8] J.H. Kwak, L. Kovarik, J. Szanyi, CO_2 reduction on supported Ru/Al_2O_3 catalysts: cluster size dependence of product selectivity, ACS Catal. 3 (2013) 2449–2455.

[9] X. Wang, Y. Hong, H. Shi, J. Szanyi, Kinetic modeling and transient DRIFTS-MS studies of CO_2 methanation over Ru/Al_2O_3 catalysts, J. Catal. 343 (2016) 185–195.

[10] Y. Yan, Q. Wang, C. Jiang, Y. Yao, D. Lu, J. Zheng, Y. Dai, H. Wang, Y. Yang, Ru/Al_2O_3 catalyzed CO_2 hydrogenation: oxygen-exchange on metal support interfaces, J. Catal. 367 (2018) 194–205.

[11] G. Garbarino, C. Wang, T. Cavattoni, E. Finocchio, P. Riani, M. Flytzani-Stephanopoulos, G. Busca, A study of Ni/La-Al_2O_3 catalysts: a competitive system for CO_2 methanation, Appl. Catal. B Environ. 248 (2019) 286–297.

[12] Q. Liu, Z. Zhong, F. Gu, X. Wang, X. Lu, H. Li, G. Xu, F. Su, CO methanation on ordered mesoporous Ni-Cr-Al catalysts: effects of the catalyst structure and Cr promoter on the catalytic properties, J. Catal. 337 (2016) 221–232.

[13] F. Song, Q. Zhong, Y. Yu, M. Shi, Y. Wu, J. Hu, Y. Song, Obtaining well-dispersed Ni/Al_2O_3 catalyst for CO_2 methanation with a microwave-assisted method, Int. J. Hydrogen Energy 42 (2017) 4174–4183.

[14] D. Beierlein, D. Häussermann, M. Pfeifer, T. Schwarz, K. Stöwe, Y. Traa, E. Klemm, Is the CO_2 methanation on highly loaded Ni-Al_2O_3 catalysts really structure-sensitive? Appl. Catal. B Environ. 247 (2019) 200–219.

[15] C. Sun, K. Swirk, D. Wierzbicki, M. Motak, T. Grzybek, P. Da Costa, On the effect of yttrium promotion on Ni-layered double hydroxides-derived catalysts for hydrogenation of CO_2 to methane, Int. J. Hydrogen Energy 43 (2021) 12169–12179.

[16] S. Navarro-Jaén, J.C. Navarro, L.F. Bobadilla, M.A. Centeno, O.H. Laguna, J. A. Odriozola, Size-tailored Ru nanoparticles deposited over γ-Al_2O_3 for the CO_2 methanation reaction, Appl. Surf. Sci. 483 (2019) 750–761.

[17] S. Gudyka, G. Grzybek, J. Grybos, P. Indyka, B. Leszczynski, A. Kotarba, Z. Sojka, Enhancing the deN_2O activity of the supported Co_3O_4|α-Al_2O_3 catalyst by glycerol-assisted shape engineering of the active phase at the nanoscale, Appl. Catal. B Environ. 201 (2017) 339–347.

[18] W. Wang, S. Wang, X. Ma, J. Gong, Recent advances in catalytic hydrogenation of carbon dioxide, Chem. Soc. Rev. 40 (2011) 3703–3727.

[19] J.M. Rynkowski, T. Paryjczak, M. Lenik, Characterization of alumina supported nickel-ruthenium systems, Appl. Catal. A Gen. 126 (1995) 257–271.

[20] S. Kikkawa, K. Teramura, H. Asakura, S. Hosokawa, T. Tanaka, Isolated platinum atoms in Ni/γ-Al_2O_3 for selective hydrogenation of CO_2 toward CH_4, J. Phys. Chem. C 123 (2019) 23446–23454.

[21] K. Ray, G. Deo, A potential descriptor for the CO_2 hydrogenation to CH_4 over Al_2O_3 supported Ni and Ni-based alloy catalysts, Appl. Catal. B Environ. 218 (2017) 525–537.

[22] S. Tada, D. Minori, F. Otsuka, R. Kikuchi, K. Osada, K. Akiyama, S. Satokawa, Effect of Ru and Ni ratio on selective CO methanation over Ru-Ni/TiO_2, Fuel 129 (2014) 219–224.

[23] C. Yuan, N. Yao, X. Wang, J. Wang, D. Lv, X. Li, The SiO_2 supported bimetallic Ni-Ru particles: a good sulfur-tolerant catalyst for methanation reaction, Chem. Eng. J. 260 (2015) 1–10.

[24] K.K. Mohaideen, W. Kim, K.Y. Koo, W.L. Yoon, Highly dispersed Ni particles on Ru/NiAl catalyst derived from layered double hydroxide for selective CO methanation, Catal. Commun. 60 (2015) 8–13.

[25] S. Li, D. Gong, H. Tang, Z. Ma, Z.-T. Liu, Y. Liu, Preparation of bimetallic Ni@Ru nanoparticles supported on SiO_2 and their catalytic performance for CO methanation, Chem. Eng. J. 334 (2018) 2167–2178.

[26] Q. Liu, S. Wang, G. Zhao, H. Yang, M. Yuan, X. An, H. Zhou, Y. Qiao, Y. Tian, CO_2 methanation over ordered mesoporous NiRu-doped CaO-Al_2O_3 nanocomposites with enhanced catalytic performance, Int. J. Hydrogen Energy 43 (2018) 239–250.

[27] L. Wei, N. Kumar, W. Haije, J. Peltonen, M. Peurla, H. Grénman, W. de Jong, Can bi-funtional nickel modified 13X and 5A zeolite catalysts for CO_2 methanation be improved by introducing ruthenium? Mol. Catal. 494 (2020), 111115.

[28] A. Solis-Garcia, J.F. Louvier-Hernandez, A. Almendarez-Camarillo, J.C. Fierro-Gonzalez, Participation of surface bicarbonate, formate and methoxy species in the carbon dioxide methanation catalyzed by ZrO_2-supported Ni, Appl. Catal. B Environ. 218 (2017) 611–620.

[29] C. Vogt, E. Groeneveld, G. Kamsma, M. Nachtegaal, L. Lu, C.J. Kiely, P.H. Berben, F. Meirer, B.M. Weckhuysen, Unravelling structure sensitivity in CO_2 hydrogenation over nickel, Nat. Catal. 1 (2018) 127–134.

[30] C. Liang, L. Zhang, Y. Zheng, S. Zhang, Q. Liu, G. Gao, D. Dong, Y. Wang, L. Xu, X. Hu, Methanation of CO_2over nickel catalysts: Impacts of acidic/basic sites on formation of the reaction intermediates, Fuel 262 (2020), 116521.

[31] J.A.H. Dreyer, P. Li, L. Zhang, G.K. Beh, R. Zhang, P.H.-L. Sit, W.Y. Teoh, Influence of the oxide support reducibility on the CO_2 methanation over Ru-based catalysts, Appl. Catal. B Environ. 219 (2017) 715–726.

[32] A. Cárdenas-Arenas, A. Quindimil, A. Davó-Quiñonero, E. Bailón-García, D. Lozano-Castelló, U. De-La-Torre, B. Pereda-Ayo, J.A. González-Marcos, J. R. González-Velasco, A. Bueno-López, Isotopic and in situ DRIFTS study of the CO_2 methanation mechanism using Ni/CeO_2 and Ni/Al_2O_3 catalysts, Appl. Catal. B Environ. 265 (2020) 118538.

[33] A. Westermann, B. Azambre, M.C. Bacariza, I. Graça, M.F. Ribeiro, J.M. Lopes, C. Henriques, Insigth into CO_2 methanation mechanism over NiUSY zeolites: an operando IR study, Appl. Catal. B Environ. 174-175 (2015) 120–125.

[34] A. Quindimil, U. De-La-Torre, B. Pereda-Ayo, A. Davó-Quiñonero, E. Bailón-Gracía, D. Lozano-Castelló, J.A. González-Marcos, A. Bueno-López, J.R. González-Velasco, Effect of metal loading on the CO_2 methanation: a comparison between alumina supported Ni and Ru catalysts, Catal. Today 356 (2020) 419–432.

[35] A. Borodzinski, Magdalena Bonarowska, Relation between crystalline size and dispersion on supported metal catalysts, Langmuir 13 (1997) 5613–5620.

[36] C. Jiménez-González, Z. Boukha, B. de Rivas, J.J. Delgado, M.A. Cauqui, J. R. González-Velasco, J.I. Gutiérrez-Ortiz, R. López-Fonseca, Structural characterization of Ni/alumina reforming catalysts activated at high temperatures, Appl. Catal. A Gen. 466 (2013) 9–20.

[37] A. Morales-Marín, J.L. Ayastuy, U. Iriarte-Velasco, M.A. Gutiérrez-Ortiz, Nickel aluminate spinel-derived catalysts for the aqueous phase reforming of glycerol: effect of reduction temperature, Appl. Catal. B Environ. 244 (2019) 931–945.

[38] C. Ding, J. Wang, G. Ai, S. Liu, P. Liu, K. Zhang, Y. Han, X. Ma, Partial oxidation of methane over silica supported Ni nanoparticles with size control by alkanol solvent, Fuel 175 (2016) 1–12.

[39] A. Cárdenas-Arenas, A. Quindimil, A. Davó-Quiñonero, E. Bailón-García, D. Lozano-Castelló, U. De-La-Torre, B. Pereda-Ayo, J.A. González-Marcos, J. R. González-Velasco, A. Bueno-López, Design of active sites in Ni/CeO_2 catalysts for the methanation of CO_2: tailoring the Ni-CeO_2 contact, Appl. Mater. Today 19 (2020), 100591.

[40] M. Kourtelesis, P. Panagiotopoulou, X.E. Verykios, Influence of structural parameters on the reaction of low temperature ethanol steam reforming over Pt/Al_2O_3 catalysts, Catal. Today 258 (2015) 247–255.

[41] D. Duprez, P. Pereira, A. Miloudi, R. Maurel, Steam dealkylation of aromatic hydrocarbons: II. Role of the support and kinetic pathway of oxygenated species in toluene steam dealkylation over group VIII metal catalysts, J. Catal. 75 (1982) 151–163.

[42] S. Velu, S.K. Gangwal, Synthesis of alumina supported nickel nanoparticle catalysts and evaluation of nickel metal dispersions by temperature programmed desorption, Solid State Ion. 177 (2006) 803–811.

[43] C. Morterra, A. Zecchina, S. Coluccia, A. Chiorino, I.r. Spectroscopic study of CO_2 adsorption onto η-Al_2O_3, J. Chem. Soc. Faraday Trans. 1 (73) (1977) 1544–1560.

[44] J.I. Di Cosimo, V.K. Díez, M. Xu, E. Iglesia, C.R. Apesteguía, Structure, surface and catalytic properties of Mg-Al basic oxides, J. Catal. 178 (1998) 499–510.

[45] K. Föttinger, R. Schlögl, G. Rupprechter, The mechanism of carbonate formation on Pd-Al_2O_3 catalysts, Chem. Commun. (2008) 320–322.

[46] M.B. Jensen, S. Morandi, F. Prinetto, A.O. Sjåstad, U. Olsbye, G. Ghiotti, FT-IR characterization of supported Ni-catalysts: influence of different supports on the metal phase properties, Catal. Today 197 (2012) 38–49.

[47] Q. Pan, J. Peng, T. Sun, S. Wang, S. Wang, Insight into the reaction route of CO_2 methanation: promotion effect of medium basic sites, Catal. Commun. 45 (2014) 74–78.

[48] G. Poncelet, M.A. Centeno, R. Molina, Characterization of reduced α-alumina-supported nickel catalysts by spectroscopic and chemisorption measurements, Appl. Catal. A Gen. 288 (2005) 232–242.

[49] P. Panagiotopoulou, Hydrogenation of CO_2 over supported noble metal catalysts, Appl. Catal. A Gen. 542 (2017) 63–70.

[50] P. Panagiotopoulou, D.I. Kondarides, X.E. Verykios, Mechanistic study of the selective methanation of CO over Ru/TiO_2 catalyst: identification of active surface species and reaction pathways, J. Phys. Chem C 115 (2011) 1220–1230.

[51] T. Burger, P. Donaubauer, O. Hinrichsen, On the kinetics of the co-methanation of CO and CO_2 on a co-precipitated Ni-Al catalyst, Appl. Catal. B Environ. 282 (2021), 119408.